Review to submitted manuscript; "*Sea ice classification of TerraSAR-X ScanSAR images for the MOSAiC expedition incorporating per-class incidence angle dependency of image texture".* The manuscript investigates per-class sea ice incidence angle dependencies in TerraSAR-X ScanSAR images and GLCM textures and trains a Bayesian classifier to classify sea ice surrounding the MOSAiC expedition.

Thank you for a well written manuscript with strong English and interesting results covering a high-profile scientific campaign. To summarize the main critique points: the paper is too long, convoluted to read at times, and it is difficult to keep track of discussed subjects. In addition, parts of the methodology needs to be further clarified.

I agree with the other reviewer that the manuscript would be better suited split into two, and resubmitting them with major revisions. One manuscript could focus on the IA dependency of the TSX SC intensity and the GLCM textures, while the other could examine the GIA and the time-series of the MOSAiC campaign.

Major Comments

Disclaimer. I have limited practical experience with bayesian classifiers but extensive knowledge of deep learning with emphasis on sea ice segmentation using convolutional neural networks. Reviewing the methodology regarding the bayesian classifier raises the following concerns for me, which I would like you to consider and address:

- Limited testing (validation in your words) examples rectangles
    - 10 reference 3x3 pixels for each class is selected for each reference scene (13 scenes in total). This is a total of 1,170 pixels for each class. Considering the abundance of data at your disposal (>1,000 x >1,000 pixels in each image?), I would refrain from needle picking select small areas. Labelling data is a time consuming task but there are tools available, which could assist, e.g. https://github.com/ESA-PhiLab/iris. At least I would require a justification for the approach.
- Small size of testing rectangles
    - Why are 3 x 3 pixel rectangles selected? Could they be larger? Why not? Do the pixels have to be separate or could you label an area with multiple classes?
- Spatial and temporal biased training and testing
    - Generally training and testing should be carried out on areas without spatial or temporal correlation, i.e. on different scenes to avoid biases spilling over from the training to the testing phase. As the data is randomly split in training and test, I fear that some pixels may lie very close together, and could artificially improve the model performance but without carryover to generalization of the classifier (i.e. may not be as reliable on non-testing data).

More information on how the classifier is trained should be included. How is it optimized?

Data

The data selection should be more clearly explained or alternatively visualized using the acquisition dates. 53 scenes are used in this study, 50 during the MOSAiC campaign, 3

afterwards with low IAs to complete the spectrum. 40 of these scenes are not used for training the classifier (as I understand it). 13 of the 53 scenes have 10 3x3 rectangles labelled and used for training and testing.

Generally, when optimizing models, data is typically split into training, validation and testing and if supervised methodologies are applied, each split will have raw data (X) and a reference (Y), i.e. the “ground truth”. Typically, a validation subset should be utilized for decision making during the optimization process, i.e. should we stop (early stopping), should we tweak the learning or regularization parameters? And finally the model performance is evaluated on the test data, which no optimization changes have been made upon. As I understand the GIA training process, you are using a test subset, and should call it as such.

In regards to the segmentation tools applied, personally, I would have chosen to apply convolutional neural networks. At least it should be mentioned as a potential area of future work.

Minor Comments

L54: Why does the TSX SC data only come in the HH polarization?

L128: 10 reference rectangles of 3 x 3 pixels sounds very small. That is only 90 pixels per class per scene, i.e. 1170 pixels.
Is every class represented in every scene? And how certain are you of your qualitative selection?

L129: Improving consistency between training scenes using a 40 km x 40 km area is unclear to me. How does this work?

L180: Only textures of HH intensities have a consistent relationship with IA.. HH intensities as opposed to what? Or is it referring to the scaling of the image, i.e. dB.

L337: ‘On the contrary..’ This sentence is quite difficult to read. I think it should be split up into two sentences.

In addition, there is a pdf document attached with grammatical suggests.

https://doi.org/10.5194/tc-2022-86
Preprint. Discussion started: 3 May 2022

The Cryosphere Discussions
Open Access
EGU

Sea ice classification of TerraSAR-X ScanSAR images for the MOSAiC expedition incorporating per-class incidence angle dependency of image texture

Wenkai Guo[1], Polona Itkin[1], Suman Singha[2], Anthony Paul Doulgeris[1], Malin Johansson[1], and Gunnar Spreen[3]

[1]Department of Physics and Technology, UiT The Arctic University of Norway
[2]Maritime Safety and Security Laboratory, Remote Sensing Technology Institute (IMF), German Aerospace Center (DLR), 28359 Bremen, Germany
[3]Institute of Environmental Physics, University of Bremen

Correspondence: Wenkai Guo (wenkai.guo@uit.no)

Abstract.

In this study, we provide sea ice classification maps of a sub-weekly time series of X-band TerraSAR-X ScanSAR (TSX SC, HH polarization) images from November 2019 to March 2020 covering the Multidisciplinary drifting Observatory for the Study of Arctic Climate (MOSAiC) expedition. This classified time series benefits from the wide spatial coverage and relatively high spatial resolution of the TSX SC dataset, classifying sea ice into leads, young ice with different intensities, and thick ice with different degrees of deformation. We use a classification method considering per-class incidence angle (IA) dependencies (the Gaussian IA classifier) to correct the IA effect (decreasing backscatter with increasing IAs) specific to each class. In addition to HH intensities, we use Gray-Level Co-occurrence Matrix (GLCM) textures as input features to aid the task of one-band classification. Accordingly, we investigate and demonstrate IA dependencies of TSX SC intensities and image textures for different sea ice classes, which are found to be generally lower than those for C-band SAR data. Optimal parameters for GLCM texture calculation are derived to achieve good separation between class distributions while keeping maximum spatial detail and minimizing texture collinearity. Class probabilities yielded from the GIA classifier are further adjusted by a Markov Random Field (MRF) contextual smoothing process to generate final classification results. A significant increase in classification performance is achieved from the inclusion of textures with optimized parameters, as evaluated by classification accuracies (final overall accuracy: 86.05%) and comparison to sea ice roughness derived from sea ice thickness measurements (correspondence consistently close to or higher than 80%). Areal fractions of classes representing ice openings (leads and young ice) correspond well with ice opening time series derived from *in situ*, satellite SAR and optical data in this and previous studies. This study provides a SAR perspective on the changing sea ice conditions surrounding the MOSAiC ice camp through the expedition, and a useful basic dataset for future MOSAiC studies on physical sea ice processes and ocean and climate modeling.

https://doi.org/10.5194/tc-2022-86
Preprint. Discussion started: 3 May 2022


The Cryosphere Discussions

1 Introduction

During the one-year-long Multidisciplinary drifting Observatory for the Study of Arctic Climate (MOSAiC) expedition from 2019 to 2020, the icebreaker RV Polarstern drifted with sea ice along the Transpolar Drift in the Central Arctic, conducting the largest multidisciplinary Arctic research expedition in history. Satellite data acquisitions from multiple platforms were coordinated to survey the broader sea ice area surrounding the expedition, enabling continuous large-scale monitoring of physical sea ice conditions along the drift. Also, extensive on-ice, airborne and ship-based *in situ* data was collected surrounding the MOSAiC ice floe, where Polarstern was moored and the Central Observatory (CO) established. These include data from meteorological stations, airborne laser surveys, ship radar measurements, and a distributed network of autonomous buoys, etc (Krumpen and Sokolov, 2020; Nicolaus et al., 2021; Shupe et al., 2022). This expedition aimed to facilitate detailed physical, biogeochemical and ecological studies of the region, enabling multi-scale quantification of relevant processes and feedbacks and eventually the production of improved climate and Earth system models (Krumpen et al., 2021; Nicolaus et al., 2021; Shupe et al., 2022). The classification of sea ice types is an important basic representation of sea ice conditions which supports various types of further analyses, e.g., monitoring ice break-up and lead formation, inferring the occurrence of sea ice deformation, studying ice-associated and under-ice ecology, and as input to ocean and climate models, etc.

Satellite Synthetic Aperture Radar (SAR) data has been used widely for sea ice classification for operational and scientific purposes due to its high spatial resolution and weather- and illumination-independent monitoring capabilities (Zakhvatkina et al., 2019). Coordinated acquisitions of TerraSAR-X ScanSAR (TSX SC) data were conducted to specifically provide consistent coverage of the MOSAiC ice floe throughout the expedition. This dataset provides daily X-band (9.65 GHz) imaging with 8.25 m nominal pixel spacing (considerably higher than open-access ScanSAR products, e.g., Sentinel-1 (S1)), and an extent of approximately 100×150 km, and is a valuable data source for long-term examination of sea ice development for MOSAiC. This study aims to produce a classified winter (November 2019 to March 2020) time series of TSX SC data surrounding the CO, which can serve as a basis for further MOSAiC sea ice studies and modeling efforts.

TSX SC scenes in this time series cover a wide range of incidence angles (IAs). Therefore, appropriate adjustment for the IA effect of SAR signal (generally decreasing backscatter intensities with IA) is crucial for reliable and consistent classification of the time series. It has been demonstrated that the magnitude of the IA effect varies with sea ice types (Mäkynen et al., 2002; Mäkynen and Juha, 2017; Mahmud et al., 2018). This phenomenon necessitates per-class correction of the IA effect. Therefore, a SAR sea ice classifier which considers between-class IA dependency differences is used in this study. Named the Gaussian Incidence Angle (GIA) classifier, it directly incorporates per-class IA dependencies into a Bayesian classifier, treating the IA dependence as a class property instead of an image property. This is achieved by replacing the constant mean vector of the Gaussian probability density function with a linearly variable mean (Lohse et al., 2020). This classifier has been developed for use with S1 ExtraWide (EW) data, and has also be used with Radarsat-2 ScanSAR Wide and Fine Quad-pol (RS2 SCW and FQ) data with minor adjustments (Guo et al., 2022). The GIA classifier reliably corrects the IA effect on HH and HV channels of these datasets, resulting in improved classification results compared to classification on scenes with global IA correction.

https://doi.org/10.5194/tc-2022-86
Preprint. Discussion started: 3 May 2022

TSX SC data used in this study comes in the HH polarization. The same ice types can have vastly different HH intensities due to different surface characteristics, e.g., different degrees of deformation on FYI and MYI, and different surface roughness and salinity levels on young ice, etc. On the other hand, some ice types have been shown to have similar X-band HH intensities, e.g., deformed first-year ice (FYI), multi-year ice (MYI) and young ice (e.g., Liu et al. 2016). Therefore, in addition to HH intensities, we use Gray-Level Co-occurrence Matrix (GLCM) texture measures as input to the classification to expanded the feature space. In the logarithmic (dB) domain, S1 EW textures of the HH channel for open water and different ice types generally have a linear relationship with IA (Lohse et al., 2021). To our knowledge, no previous study has demonstrated IA dependencies of different Arctic sea ice types for TSX SC intensities and GLCM textures. This study examines the statistical distributions of HH intensities and textures of TSX SC scenes in the MOSAiC winter time series, and evaluates their IA dependencies and hence applicability as input features to the GIA classifier.

The optimal texture window size and set of texture measures to use for texture calculation are derived to provide statistical separability between class distributions, which is evaluated by the Kolmogorov-Smirnov (K-S) distance (Massey Jr, 1951). For better general applicability of our proposed classification workflow, 17 GLCM texture measures are analyzed which are derivable using commonly available software and online tools, i.e., ESA SNAP (European Space Agency, 2020) and the Google Earth Engine (GEE, Gorelick et al. 2017). As we aim to fully utilize the spatial resolution provided by TSX SC data, a rating system is developed to find the set of texture measures that provides separability between classes at the smallest possible window sizes, while minimizing inter-correlations.

In summary, the objectives of this study are: 1. to investigate and demonstrate per-class IA dependencies of TSX SC HH intensity and GLCM textures, based on which to determine the feasibility and optimal parameterization of including texture measures as input features to the GIA classifier; 2. to train the GIA classifier to produce a classified winter time series for the sea ice area surrounding the MOSAiC expedition.

2 Materials and methods

Materials and methods used in this study are summarized in Fig. 1, and explained as follows.

2.1 Data

This study uses 50 scenes during the MOSAiC winter (2019.11.01 to 2020.03.28, IA: 31.90˚to 59.56˚) for the examination of IA dependencies of HH intensities and textures, and sea ice classification (hereafter referred to as the time series), with an average of 3 scenes per week. Additionally, 3 scenes are picked from 2020.03.31 onward (2020.03.31, 2020.04.03 and 2020.04.11, IA: 17.18˚to 36.70˚) and are only used for the demonstration of IA dependency of HH intensities, which completes the coverage of the full IA range of TSX SC data. All scenes are radiometrically corrected and calibrated to σ^0 and subjected to a speckle filter (boxcar, 3×3), and then converted to dB. Fig. 2(b) shows the scene boundaries, and Fig. 2(c) shows their IA ranges.

https://doi.org/10.5194/tc-2022-86
Preprint. Discussion started: 3 May 2022

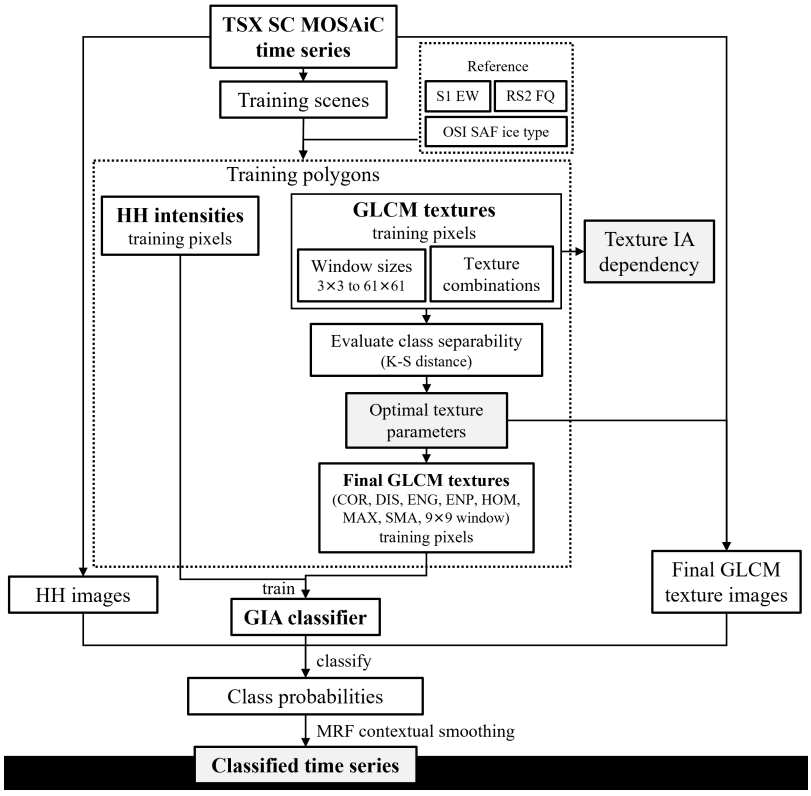

Figure 1. Materials and methods.

Scenes after 2020.03.31 were captured at low IAs (Fig. 2(c)) to keep the CO, which was drifting below 85.5°N (Fig. 2(b)), within the scene frames, and exhibit consistent linear IA dependency with other scenes for HH intensities but not for HH textures (not shown). The spatial details obtainable from these scenes are different from others after being subjected to identical pre-processing steps, resulting in considerably different texture values. Additionally, these scenes generally have higher noise floors than the rest of the scenes, and are thus more affected by noise (Fritz et al., 2013). Therefore, they are useful for the investigation of IA dependencies of TSX SC intensities for lower IAs, but not for deriving a consistent texture-based classifier for winter MOSAiC.

Environmental conditions are inferred from 2m air temperature records extracted from the weather station MetCity in the CO (Fig. 2(c)), which show that the temperatures remained mostly below $-5^{\circ}C$ throughout the study period except for late April, when warm spells brought temperatures to near $0^{\circ}C$. A subset of TSX SC scenes are selected in freezing conditions (reference scenes), from which reference polygons are derived for training, validation, and the examination of IA dependencies. A total of 13 reference scenes (plotted in Fig. 2(c) and shown in detail in Fig. 3(b)) are chosen to cover each month between November 2019 and April 2020 and the whole IA range of TSX SC data (17.18°to 59.56°). Among these, scenes before 2020.03.31 are used for training and validation (training scenes).

https://doi.org/10.5194/tc-2022-86
Preprint. Discussion started: 3 May 2022

For the reference scenes, cloud-free pixels from the National Snow and Ice Data Center (NSIDC) MOD29/MYD29 sea ice surface temperatures (IST) dataset (Hall and Riggs., 2021) are extracted to show temperatures within the scene boundaries. For each reference scene, the IST scene with maximum cloud-free overlap (> 70% of the scene area) within 3 hours of TSX SC acquisition is manually selected and used to ensure that ISTs are well below -5˚(Fig. 2(d)). Overlapping S1 EW and RS2 FQ scenes and the Ocean and Sea Ice Satellite Application Facility (OSI SAF) sea ice type (OSI-403-d, Fig. 2(a)) product (OSI SAF, 2019) are used qualitatively as visual reference to aid the derivation of reference polygons, providing general knowledge about large-scale ice conditions and comparison with C-band SAR signals, respectively.

2.2 Reference polygons of sea ice classes

We classify sea ice into leads, rough young ice with different HH intensities, and thick ice (FYI or MYI) with different roughness levels. This is explained in details below, where intensity thresholds are visually derived approximate values only used as one of the criteria in deriving the reference polygons:

1. Leads: ice openings occupied by calm open water, nilas or smooth newly formed ice, having the lowest HH intensities (< -25 dB). The separation between open water in different wind states is not within the scope of this study, and visual examination shows that open water leads in the TSX SC time series are all narrow ($\leq 250m$) and predominantly in a calm state.

2. Dark young ice (DYI): rough, newly formed ice surfaces in open leads with relatively high HH intensities (≥ -15 dB) are all regarded as young ice, irrespective of ice thickness. Young ice is further split into two separate classes to aid the classification of single-band TSX SC data. This is only done to account for areas with distinctive difference in HH intensities, presumably due to the evolving surface roughness, e.g., influenced by the growing and disappearing of frost flowers which are highly saline and causes changing scales of surface roughness through time, thus strongly impacting X-band SAR signals (Martin et al., 1995; Barber et al., 2014; Isleifson et al., 2018; Johansson et al., 2018). The separated young ice classes do not correspond to existing ice types given in the WMO nomenclature (WMO, 2018). The DYI class includes young ice areas with comparatively low HH intensities (between -15 dB and -10 dB).

3. Bright young ice (BYI): rough young ice with HH intensities of greater than -10 dB.

4. Level ice (LI): smooth thick ice (FYI or MYI) areas having intermediate HH intensities, between leads and DYI (-25 dB and -15 dB).

5. Deformed ice (DefI): rough thick ice with HH intensities between -15 dB and -10 dB.

6. Heavily deformed ice (HDefI): thick ice areas with very high degrees of deformation, thus having high HH intensities (≥ -10 dB).

For each class, 10 reference rectangles of 3×3 pixels are manually derived for each reference scene. Polygons of each class in each scene are then randomly split in half to be used for training and validation. To improve the consistency of training across scenes, polygons of LI, DefI and HDefI in a roughly 40 km$\times$40 km area surrounding the CO are derived for approximately the 'same ice' for all reference scenes, considering the shift in the position of the CO relative to scene borders. Fig. 3(a) shows example reference polygons derived for the scene on 2019.11.22.

https://doi.org/10.5194/tc-2022-86
Preprint. Discussion started: 3 May 2022

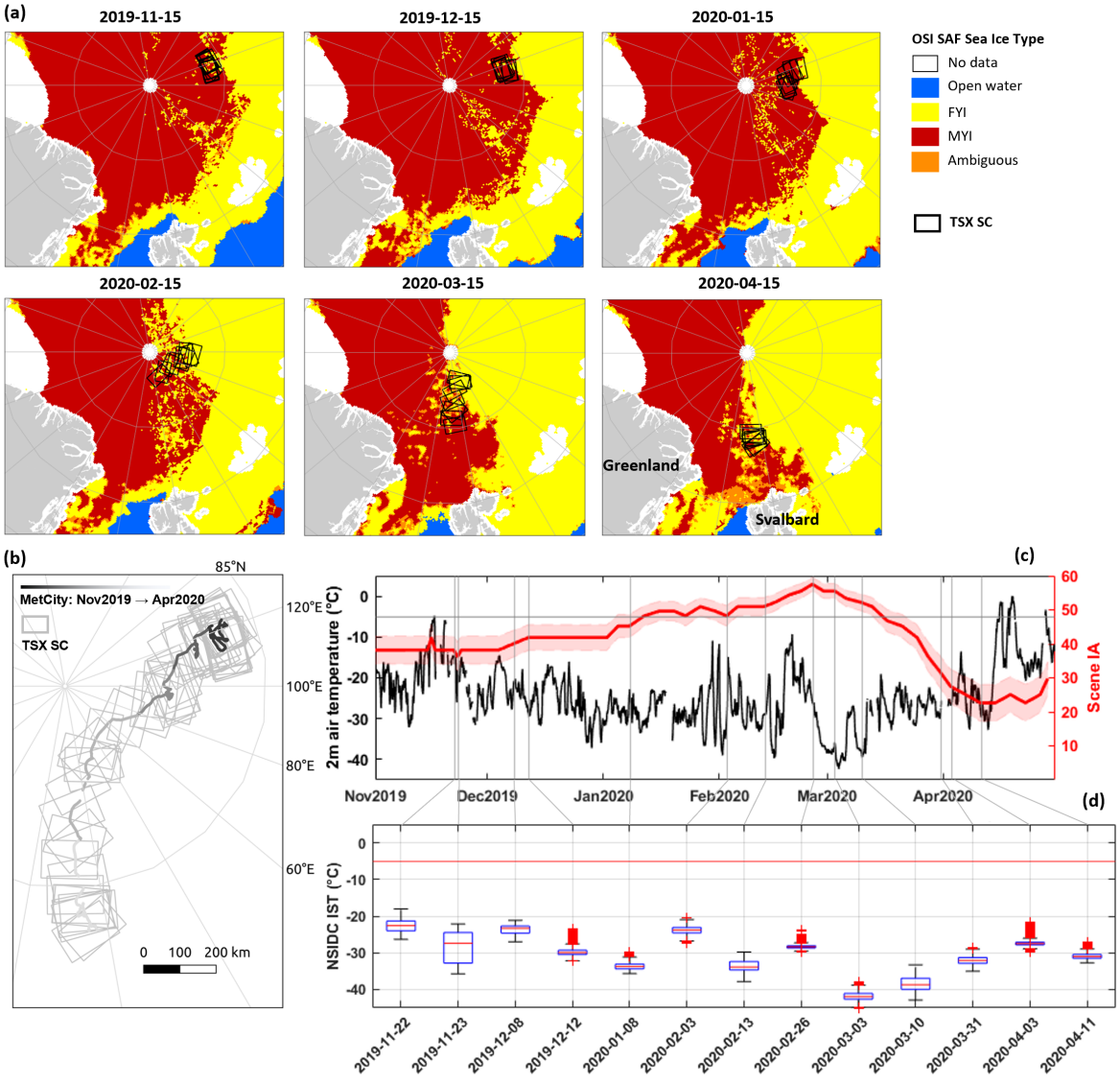

Figure 2. (a) TSX SC scenes in each month and OSI SAF sea ice classifications of surrounding sea ice areas in the middle of each month; (b) drift track of the weather station MetCity and its relative position to TSX SC scenes (c) 2m air temperature records through the study period and IA ranges of TSX scenes (average IAs in red line), with vertical lines representing selected reference scenes; (d) box-plots of NSIDC IST within each reference scene, where boxes cover the 25^{th} to the 75^{th} percentile with the median shown as the red bar. Whiskers extend to data extremes excluding outliers, and red crosses indicate outliers.

Fig. 4 shows an example of the progression of young ice on overlapping TSX SC and S1 EW scenes, both displaying the HH channel. High winds were observed during this period (Krumpen et al., 2021), which presumably contributed to large ice opening and deformation events. One day prior to the example scenes (2019.11.20), wide-spread lead openings of open

https://doi.org/10.5194/tc-2022-86
Preprint. Discussion started: 3 May 2022

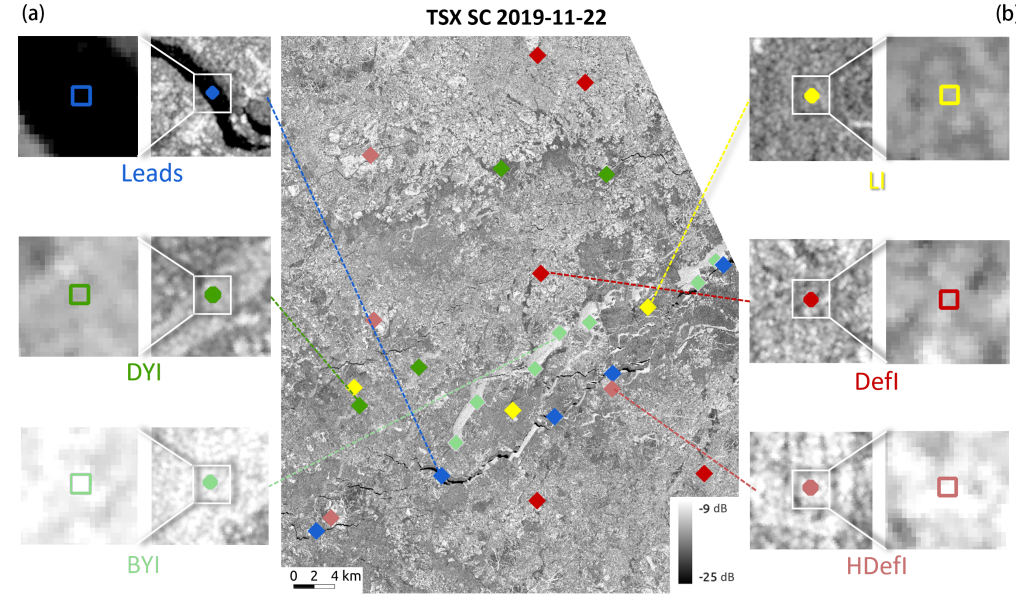

(b)

Scene date	IA range
20200411	17.2 - 28.1
20200403	22.4 - 32.5
20200331	27.3 - 36.7
20191123	31.9 - 40.5
20191122	34.0 - 42.3
20191208	36.1 - 44.0
20191212	38.1 - 45.6
20200108	41.8 - 48.6
20200203	45.2 - 51.3
20200213	48.3 - 53.6
20200310	49.7 - 54.7
20200303	53.3 - 57.7
20200226	55.5 - 59.6

Figure 3. (a) example reference polygons of different classes over the TSX SC scene on 2019.11.22; (b) dates and IA ranges of reference scenes. All subsequent figures of HH intensities use the dB range shown here.

water or nilas can be seen. Between 2019.11.20 and 2019.11.21, even more openings appeared which quickly re-froze into young ice. On the scene on 2019.11.21, most young ice appear very bright (thus belonging to the BYI class). While the leads gradually close up, these young ice areas gradually darken in TSX SC scenes until they reach a similar level of HH intensities to the surrounding ice. On the other hand, on S1 EW scenes, HH intensities for young ice gradually increase, from similar or lower brightness to nearby LI to very bright on the 2019.11.23 and 2019.11.24, until they again reach similar brightness to LI later. This delayed increase and decrease in SAR intensities of young ice in C-band (5.405 GHz) compared to X-band (9.65 GHz) data is presumably due to different interactions between changing surface roughness scales and SAR signals of different wavelengths (Isleifson et al., 2010; Dierking, 2010; Barber et al., 2014; Park et al., 2020). This distinct difference in young ice intensities in the HH channel through time confirms the need for separating young ice into two classes for this study.

2.3 IA dependency examination of HH intensities and textures

2.3.1 GLCM textures

For the purpose of using image textures as features in sea ice classification, second-order texture measures (considering the relationship between groups of two pixels) are analyzed in this study, which are calculated on the basis of the gray-level co-occurrence matrix (GLCM, Haralick et al. 1973). The GLCM tabulates how different combinations of gray-levels co-occur in pre-defined image windows, based on which statistical measures are derived to represent local spatial variations surrounding the central pixel. GLCM textures are among the most powerful texture discrimination tools (Barber and LeDrew,

https://doi.org/10.5194/tc-2022-86
Preprint. Discussion started: 3 May 2022

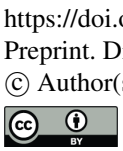

The Cryosphere Discussions
Open Access
EGU

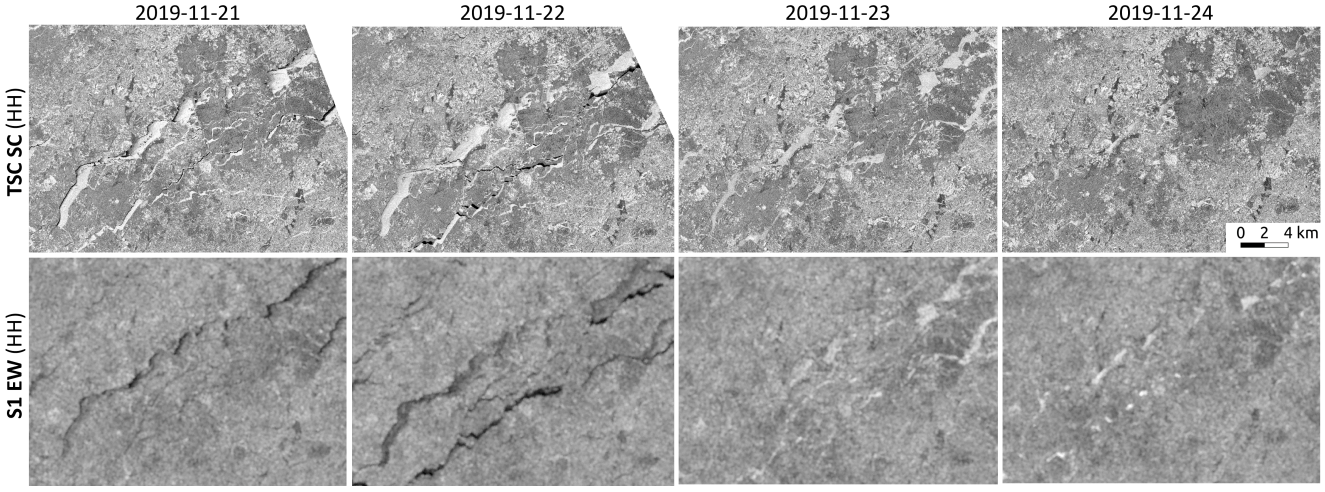

Figure 4. Progression of young ice on coincident TSX SC and S1 EW scenes (both on the HH channel), all scaled by the same range of intensities through the 4-day period.

1991; Zakhvatkina et al., 2019), and have been widely used for texture-based classification of remote sensing images in general (Hall-Beyer, 2017), and specifically for sea ice classification of both X- and C-band SAR data (e.g., Clausi and Yu 2004; Leigh et al. 2014; Zakhvatkina et al. 2017; Murashkin et al. 2018; Park et al. 2020; Lohse et al. 2021; and those listed in Table 2). Compared to classification based only on SAR backscatter intensities, they have been shown to provide additional separability between FYI and MYI, young ice and MYI, and level and deformed ice (e.g., Holmes et al. 1984; Shokr 1991; Leigh et al. 2014; Zakhvatkina et al. 2017; Lohse et al. 2021).

For TSX data, Ressel et al. (2015) used 5 GLCM textures calculated from the VV channel of 3 TSX SC images to classify sea ice near Svalbard with an artificial neural network (ANN), and reported satisfactory classification results for scenes with similar IA ranges to the training scene. Liu et al. (2016) used 8 GLCM textures from TSX SC and Wide ScanSAR (WSC) as features to classify sea ice on the east coast of Antarctica, using IA directly as an input feature to a support vector machine (SVM) classifier. To reduce scalloping and inter-scan banding issues in ScanSAR images, Zhang et al. (2019) used a combination of Kalman filter, 5 GLCM textures and SVM on 5 TSX SC (HH/VV) scenes, and Liu et al. (2021) used the same 5 GLCM textures in two spatial scales from 8 TSX SC/WSC (HH) scenes to classify sea ice, both in the Beaufort Sea, with no corrections for the IA effect. In this study, we examine the separability between sea ice classes provided by 17 commonly achievable GLCM textures (through ESA SNAP and GEE) calculated from TSX SC HH intensities, supported by the examination of their IA dependencies. This enables us to find an optimal way of using GLCM textures as input features into the GIA classifier, and classify sea ice for the MOSAiC drift with reliable correction of the IA effect. The GLCM textures used are listed in Table 1, where the mathematical expressions match those from Haralick et al. (1973) and Conners and Harlow (1980).

Texture windows surrounding the training pixels can potentially cover mixed classes. This is especially true for classes that are spatially confined, namely classes representing 'lead ice' (leads, DYI and BYI), and also HDefI. The former usually takes

https://doi.org/10.5194/tc-2022-86
Preprint. Discussion started: 3 May 2022

The Cryosphere Discussions
Open Access
EGU

Table 1. GLCM texture measures used analyzed in this study.

(1) Cluster Prominence (CLP): $\sum_i \sum_j (i + j - \mu_i - \mu_j)^4 P_{i,j}$	(10) Homogeneity (HOM): $\sum_i \sum_j \frac{P_{i,j}}{1+(i-j)^2}$
(2) Cluster Shade (CLS): $\sum_i \sum_j (i + j - \mu_i - \mu_j)^3 P_{i,j}$	(11) Information Measure of Correlation 1 (IMC1): $\frac{HXY - HXY1}{max(HX,HY)}$
(3) Contrast (CON): $\sum_i \sum_j P_{i,j} (i - j)^2$	(12) Information Measure of Correlation 2 (IMC2): $\sqrt{(1 - \exp(-2.0(HXY2 - HXY)))}$
(4) Correlation (COR): $\frac{\sum_i \sum_j ij P_{i,j} - \mu_x \mu_y}{\sigma_x \sigma_y}$	(13) Maximum Probability (MXP): $\max(P_{i,j})$
(5) Difference Entropy (DFE): $-\sum_{i=0}^{N_g - 1} P_{x-y}(i) \log P_{x-y}(i)$	(14) Mean (MEAN): $\sum_i \sum_j iP_{i,j}$
(6) Difference Variance (DFV): $\sum_{i=2}^{2N_g} \left(i - \left[\sum_{i=2}^{2N_g} iP_{x-y}(i)\right]\right)^2$	(15) Sum Average (SMA): $\sum_{i=2}^{2N_g} iP_{x+y}(i)$
(7) Dissimilarity (DIS): $\sum_i \sum_j P_{i,j} \lvert i - j \rvert$	(16) Sum Variance (SMV): $\sum_{i=2}^{2N_g} \left(i - \left[\sum_{i=2}^{2N_g} iP_{x+y}(i)\right]\right)^2$
(8) Energy (ENG): $\sqrt{\sum_i \sum_j P_{i,j}^2}$	(17) Sum of Square: Variance (VAR): $\sum_i \sum_j P_{i,j} (i - \mu)^2$
(9) Entropy (ENP): $\sum_i \sum_j P_{i,j} (-\ln P_{i,j})$	

a linear shape along ice openings, and the latter usually includes linear strips or spatially limited aggregations of deformation features, or rounded MYI floes. Therefore, in the derivation of reference polygons, an effort was made to place polygons at the center of small, rounded features and along the width of linear features. Texture windows of mixed classes can still occur for larger window sizes. Given these limitations, the maximum window sizes to guarantee the absence of mixed-class texture windows in the reference polygons in this study are 9, 25, 25, 81, 41 and 35 pixels (length of a window edge) for leads, DYI, BYI, LI, DefI and HDefI, respectively.

2.3.2 IA dependencies

In an initial examination of GLCM textures calculated from HH intensities in the linear and logarithmic (dB) domains, we found that only textures of HH intensities in dB have a consistent linear relationship with IA, given properly constrained IA range (more details below). This is one of the pre-requisites for features to be used by the GIA classifier. Similar findings are reported in (Lohse et al., 2021) for C-band S1 EW data. Thus, GLCM textures are calculated for HH intensities in dB, split into 64 gray levels (to ensure balance between precision of gray-level information and computational efficiency) with a 2-pixel

https://doi.org/10.5194/tc-2022-86
Preprint. Discussion started: 3 May 2022

offset averaged for 4 directions (0°, 45°, 90°, 135°) to avoids directional sensitivity of textures. These texture parameters are explained in Haralick et al. (1973), and in this study we use a data-driven approach to select the two most important texture parameters for the purpose of image classification: texture window size and the combination of texture measures (details shown in Section 2.3.3).

The distribution and scatter plots for HH intensities of the 13 reference scenes (IA range: of 17.18°to 59.56°, Fig. 5) show that ambiguities in HH intensities are most prominent for two class pairs: BYI vs. HDefI and DYI vs. DefI. These difficult class pairs are thus the focus of subsequent separability evaluations. The IA dependency of the leads class is the weakest among all classes (Fig. 5), being mostly under the nominal noise floor (Fritz et al., 2013) and having the widest scatter in HH intensities. HH intensities of other classes are relatively linear with IA through the whole IA range with significant slopes.

The distribution of GLCM textures calculated from dB intensities (in an example window size of 9 pixels), and their scatter plots within the IA range of the 10 training scenes (IA: 31.90°to 59.56°), are also shown in Fig. 5 (only the difficult class pairs are shown for better visual clarity). Textures generally show a weak linear relationship with IA with varying levels of dependencies (IA slopes), similar to previous C-band and X-band findings (e.g., Liu et al. 2016; Lohse et al. 2021; Scharien and Nasonova 2020). Some textures show visually apparent separability between class distributions of one or both of the difficult class pairs (e.g., DIS, ENP, MEAN, SMA, VAR) at this window size.

The classes form approximately Gaussian distributions both for HH intensities and most HH textures (Fig. 5), therefore satisfying the pre-requisites to be used as features in the GIA classifier. A considerable part of the leads class is below the nominal noise floor of the HH channel, affecting its distribution both for HH intensities and textures. Also, the leads class has distinctly different HH intensities than other classes. Therefore, leads is not included in subsequent texture-based classification. Instead, a separate classification is run for all scenes using HH intensities only, from which lead pixels are extracted and used for the final classification result, which we found to provide satisfactory lead separation.

2.3.3 Parameter optimization and calculation of GLCM textures

Optimal combination of textures and window size are selected based on class separability. Window size is a key parameter in texture-based image classification, and has been shown to influence classification accuracies more than other textural parameters (Marceau et al., 1990; Ferro and Warner, 2002). For a particular class pair, the optimal window size is dependent on the spatial scales at which unique textures of the two classes can be statistically separated. Smaller window sizes fail to include the characteristic variability of the classes, and thus prevent the separation between class distributions, while larger window sizes reduce the effective resolution of the classification result, and introduce mixed-class texture windows. Similarly, the inclusion of more texture measures generally adds to the classifier's ability to separate different classes, but the inclusion of redundant texture measures leads to increased texture collinearity and longer computational time without improving classification accuracy. The inclusion of a large number of texture measures and hence high dimensionality of the feature space additionally leads to the risk of reduced classification accuracy (Hughes, 1968; Alonso et al., 2011). Therefore, it is desirable to minimize the correlation between texture measures used for classification (Shokr, 1991; Hall-Beyer, 2008, 2017), particularly given our purpose of classifying a winter time series. In summary, the main objectives in selecting optimal texture combination and win-

https://doi.org/10.5194/tc-2022-86
Preprint. Discussion started: 3 May 2022

The Cryosphere
Discussions
Open Access
EGU

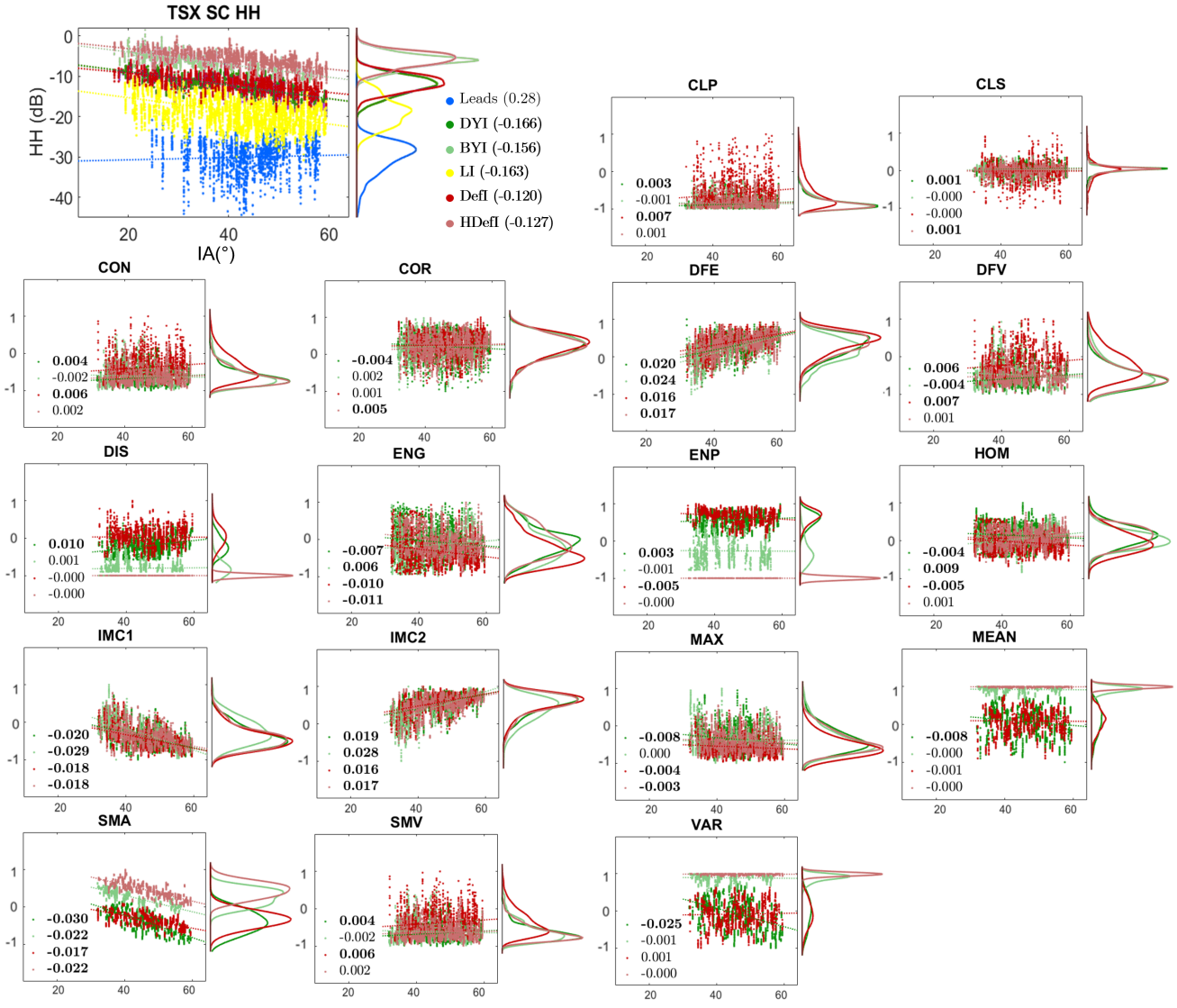

Figure 5. Histograms and scatter plots of TSX SC HH intensities with IA for the reference polygons (all classes), and GLCM textures (Table 1) with IA for the training polygons (only for DYI, DefI, BYI and HDefI for better visual clarity). Slope values of different class with IA are also shown (bold indicates statistical significance). Values of all texture measures are scaled to the -1 to 1 range to yield comparable slope values.

dow size are: 1. to provide separability between different classes, especially those having similar TSX SC HH intensities; 2. to keep a minimal window size to retain spatial details provided by the relatively high resolution of TSX SC data; 3. to reduce
220 correlation between textures used for classification.

https://doi.org/10.5194/tc-2022-86
Preprint. Discussion started: 3 May 2022

Class separability is evaluated by the K-S distance (Massey Jr, 1951), which is non-parametric and thus a relatively robust metric without assumptions of class distribution (Daniel, 1990). The K-S distance quantifies the distance between class distributions, and the K-S test yields a test decision for the hypothesis that two classes come from the same distribution. The following procedures are used to derive an optimal windows size and texture combination:

1. for each texture, K-S distance values between class pairs are calculated for all window sizes between 3 and 61 pixels for all pixels within the training polygons (training pixels);

2. for each combination of textures, the smallest window size at which all individual constituting textures provides statistical separability (evaluated by the K-S test) between all class pairs is selected as the 'optimal' window size;

3. for each texture combination at its optimal window size, the summation of K-S distance values for all textures is divided by the common logarithm of the summation of correlation coefficients between texture pairs within the combination, resulting in a 'combination rating' that provides control over texture collinearity. This rating is calculated for every texture combination from the 17 textures in Table 1;

4. texture combinations with the 10 highest ratings (in corresponding optimal window sizes) are used to classify the training scenes, and these classification results are compared visually to arrive at a final selection of texture combination and window size.

The selected optimal combination of textures is: COR, DIS, ENG, ENP, HOM, MAX and SMA. This texture combination has an optimal window size of 9 pixels. HH intensities and textures calculated accordingly for the training pixels are used to train the GIA classifier. Texture images are then calculated for all TSX SC scenes of interest and are used for final classification of the time series. GLCM texture calculation for the training pixels and the derivation of optimal texture parameters are conducted using MATLAB 2021b (The Mathworks Inc., 2021). Further production of whole texture images using HH intensities are conducted using ESA SNAP and GEE.

2.4 Classification of MOSAiC winter time series

Sea ice classification is conducted on the time series using the GIA classifier trained with HH intensities and textures with the optimal texture combination and window size (shown above). Within the classification process, a Markov Random Field (MRF) contextual smoothing component (Doulgeris, 2015) is added to alter the posterior class probabilities yielded from the GIA classifier before determining maximum probability class labels. This technique replaces global class probabilities with spatially varying local probabilities by giving more weight to class memberships of spatially neighboring classes. This process is added to reduce scattered mis-classified pixels created by the classification of texture images and also ScanSAR image artifacts including scalloping and inter-scan banding.

As the sea ice area surrounding the CO is the main focus of MOSAiC sea ice studies, in Section 3 we mainly present classification results for a 71 km×71 km square (hereafter referred to as subset A) and a 28 km×28 km square (subset B) surrounding the CO. For both subsets, a time series of areal fractions of each class is produced from the classification maps, providing a general assessment of relative changes of classes through the study period. Subset A provides results in a broad area surrounding the CO, while subset B serves to ensure a consistent sea ice area for class fraction calculation, as significant

https://doi.org/10.5194/tc-2022-86
Preprint. Discussion started: 3 May 2022

parts of subset A are often outside of TSX SC scene boundaries, resulting in the inclusion of a considerable amount of different ice surfaces when calculating class fractions.

3 Results and discussion

3.1 IA dependencies and GLCM textures - this and previous studies

IA slopes of C-band and X-band SAR backscatter intensities for different sea ice types derived in previous studies are shown in Fig. 6. Different classification schemes are used for these studies, and we summarize them into 5 commonly used classes, and display per-class IA slopes for their classes that are the most closely related to these 5 classes. There are limited number of studies reporting IA dependencies of Arctic sea ice types for X-band sensors. IA slope values shown in Liu et al. (2016), presented in blue asterisks, are derived from TSX SC and WSC scenes with a limited IA range of 22.61°to 45.31°from the east coast of Antarctica. HH intensities of TSX SC data derived in this study are generally less dependent on IA than those for C-band sensors (values summarized in Guo et al. (2022)), which is also observed in previous comparative studies of airborne X- and C-band sensors (e.g., Mäkynen and Hallikainen 2004). The general pattern of comparative IA slopes between classes is similar for C- and X-band: LI has a slightly stronger IA dependency than deformed FYI and MYI (in this study DefI and HDefI), presumably due to stronger volume scattering and added randomness in backscatter caused by deformation features for these two classes, both leading to decreased sensitivity to IA (Mäkynen et al., 2002; Dierking and Dall, 2007; Zakhvatkina et al., 2013). These differences confirm the necessity of per-class IA correction in classifying the time series.

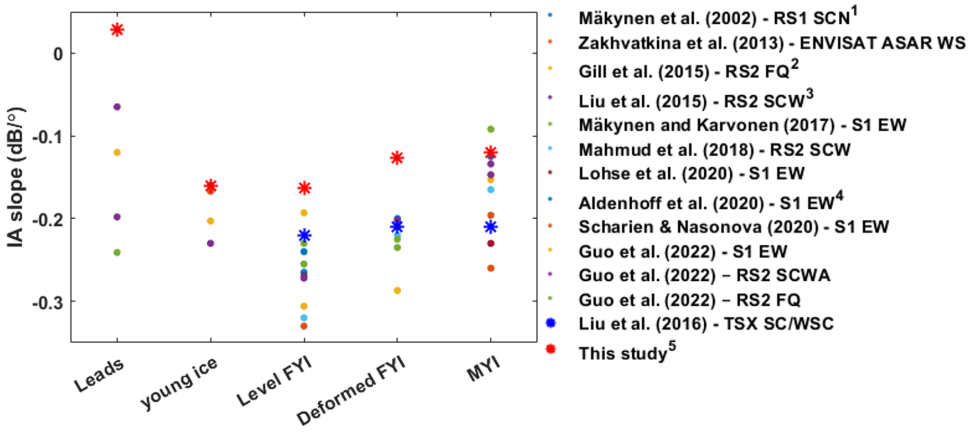

Figure 6. Comparison between IA slope values derived in this and previous studies. Dots are for C-band results, and asterisks for X-band ones. Correspondence between ice classes shown in the figure and closest ice classes in the original studies that are defined differently or more specifically: [1] FYI: FYI with dry snow on top; [2] FYI: land-fast smooth FYI with thin (7.7±3.9 cm) to thick (36.4±12.3 cm) snow cover; [3] Leads: nilas; YI: deformed gray ice; [4] MYI: averaged for MYI and old MYI; [5] YI: averaged for DYI and BYI; Deformed FYI: HDefI; MYI: DefI.

https://doi.org/10.5194/tc-2022-86
Preprint. Discussion started: 3 May 2022


The Cryosphere Discussions
Open Access
EGU

Table 2 shows GLCM texture parameters used in previous sea ice classification studies using X-band SAR. The table shows a wide variety of datasets, texture combinations and window sizes (in terms of physical length of window boundaries in meters), indicating that various GLCM textures on different geographical scales are useful for discriminating between sea ice classes. This is given that many studies use a limited number of textures measures and do not involve a process of selecting texture combinations based on class separability and texture collinearity. CON, COR, ENP and HOM are examples of frequently used textures in sea ice classification. The texture parameter selection workflow established in this study produces satisfactory classification results (Section 3.2 and Section 3.3) and is generally applicable for future studies. However, the optimal texture window size and combination yielded in this study is specific to the dataset (on the constrained IA range of the training scenes) under examination, with an aim to provide separability between classes while minimizing spatial smoothing due to texture calculation.

Table 2. Texture parameter selection in this and previous studies.

	Data				Texture parameters	
	Area	**Dataset**	**Frequency & channel**[1]	**Resolution**[2] **(m)**	**GLCM textures**[3]	**Window size**[3] **- pixel (m)**
Holmes et al. (1984)	Beaufort Sea	SURSAT SAR-580 (airborne)	X-band HV	3	CON, ENP	5 (15)
Barder & LeDrew (1991)	Mould Bay, Canada	STAR-1 (airborne)	X-band HH	6	UNI[4], COR, ENP, DIS, CON	25 (150)
Shokr (1991)	Mould Bay, Canada	STAR-1 (airborne)	X-band HH	36	CON, ENP, UNI[4], HOM, MAX	5 (180)
Liu et al. (2016)	East coast, Antarctica	TSX SC/WSC	X-band HH	15	ASM, CON, COR, DIS, ENP, HOM, MEAN, VAR	39 (585)
Ressel et al. (2015)	Barents Sea	TSX SC	X-band VV	~48	CON, DIS, ENG, ENP, HOM	11 (~528)
Zhang et al. (2019)	Barents Sea	TSX SC	X-band HH/VV	8.25	CON, COR, HOM, MEAN, VAR	39 (321.75)
Liu et al. (2021)	Beaufort Sea	TSX SC/WSC	X-band HH	8.25	CON, COR, HOM, MEAN, VAR	39 (321.75)
This study	MOSAiC Drift	TSX SC	X-band HH	8.25	COR, DIS, ENG, ENP, HOM, MAX, SMA	9 (74.25)

[1] Only SAR channels used for GLCM calculation are shown.
[2] Effective pixel spacing after pre-processing.
[3] GLCM textures and window sizes are those used for final classification.
[4] UNI: Uniformity = $\sum_i \sum_j P_{i,j}^2$, therefore similar to ENG.

3.2 Classification with HH intensities and textures

Classification results for three example scene subsets across the time series are shown in Fig. 7, where classification using HH intensities only, HH intensities and textures, and with additional application of MRF contextual smoothing are compared. Considerable classification improvement can be seen from the inclusion of GLCM textures, especially in the correct separation

https://doi.org/10.5194/tc-2022-86
Preprint. Discussion started: 3 May 2022

between the difficult class pairs. Due to ambiguities in HH intensities, classification without textures shows prevalent mixing of those class pairs. DefI and HDefI are frequently mis-classified as young ice (e.g., 2020.01.08 and 2020.03.28, zoomed-in image patches), resulting in classification maps dominated by DYI and BYI (green). Young ice is also frequently classified as DefI or HDefI (e.g., 2019.11.14, zoomed-in image patch). This issue is largely remedied by the inclusion of textures into the classification. MRF contextual smoothing further fulfills the intended purpose of eliminating scattered mis-classified pixels due to texture calculation and image artifacts, which are small in areal coverage but wide-spread, thus necessitating a smoothing process. The average overall accuracy calculated from the training scenes for classification on HH intensities and textures (82.09%) is significantly higher (p-value < 0.01) than that on HH intensities only (69.75%). The use of MRF contextual smoothing further increases (p-value < 0.01) the overall accuracy to 86.05%. The MRF contextual smoothing technique is theoretically (Doulgeris, 2015) and practically (not shown) superior to image smoothing processes without the consideration of contextual information, e.g., a local majority filter, in improving classification accuracy and minimizing the loss of spatial detail.

3.3 Winter sea ice classification time series surrounding the MOSAiC ice camp

3.3.1 Classification maps

Resulting classification maps in subset A in the middle of each month, as well as the last scene of the time series (2020.03.28), are shown in Fig. 8. The general distribution of LI vs. DefI and HDefI is consistent through the time series in the areal extent of subset A, as well as for the MOSAiC ice floe carrying the CO (zoomed-in patches). For reference, a manually derived classification of a small area around Polarstern produced by an co-author with extensive knowledge of sea ice conditions in MOSAiC is shown in Fig. 9(a). Our classification is consistent with ground observations (summarized in the manual classification map) indicating that the MOSAiC ice floe was composed of a mixture of FYI and SYI, with a strongly deformed zone in the center named 'the Fortress' (the oval-shaped ice surface classified consistently as DefI and HDefI, i.e., dark red or light red) (Krumpen et al., 2020; Itkin et al., in review). In most scenes in November 2019, part of the SYI surface in the MOSAiC ice floe surrounding the Fortress appear similar to or even darker than nearby LI (Fig. 8), thus classified as LI. This has been observed to be attributable to the presence of re-frozen melt ponds (Fig. 9(a); Krumpen et al. 2021). The classification maps clearly capture the break up and change of size and shape for the MOSAiC ice floe. Major lead openings are seen on 2020.03.17 and 2020.03.28, which are identified as BYI and DYI. Panoramic photos taken from Polarstern (Fig. 9(b), Marcel et al. 2021) confirm the presence of ice openings occupied by young ice with the same relative positioning to the ship as indicated by Fig. 8 (Polarstern circled in black in the zoomed-in patches).

The standard deviation of sea ice thickness measured from the electromagnetic induction (EM) instrument (GEM-2, Hendricks et al. 2022) along several transects near the CO are used as a combined indicator of sea ice surface and bottom roughness, and is plotted in blue on the classification maps in Fig. 10(a). Manual correction of sea ice roughness data point positions is conducted to account for sea ice drift and and geo-location errors of the sensor. The effect of ice floe rotation and deformation is still present, and the data points are averaged for windows of 4×4 TSX SC pixels (thus $33m \times 33m$) to partially remedy

https://doi.org/10.5194/tc-2022-86
Preprint. Discussion started: 3 May 2022

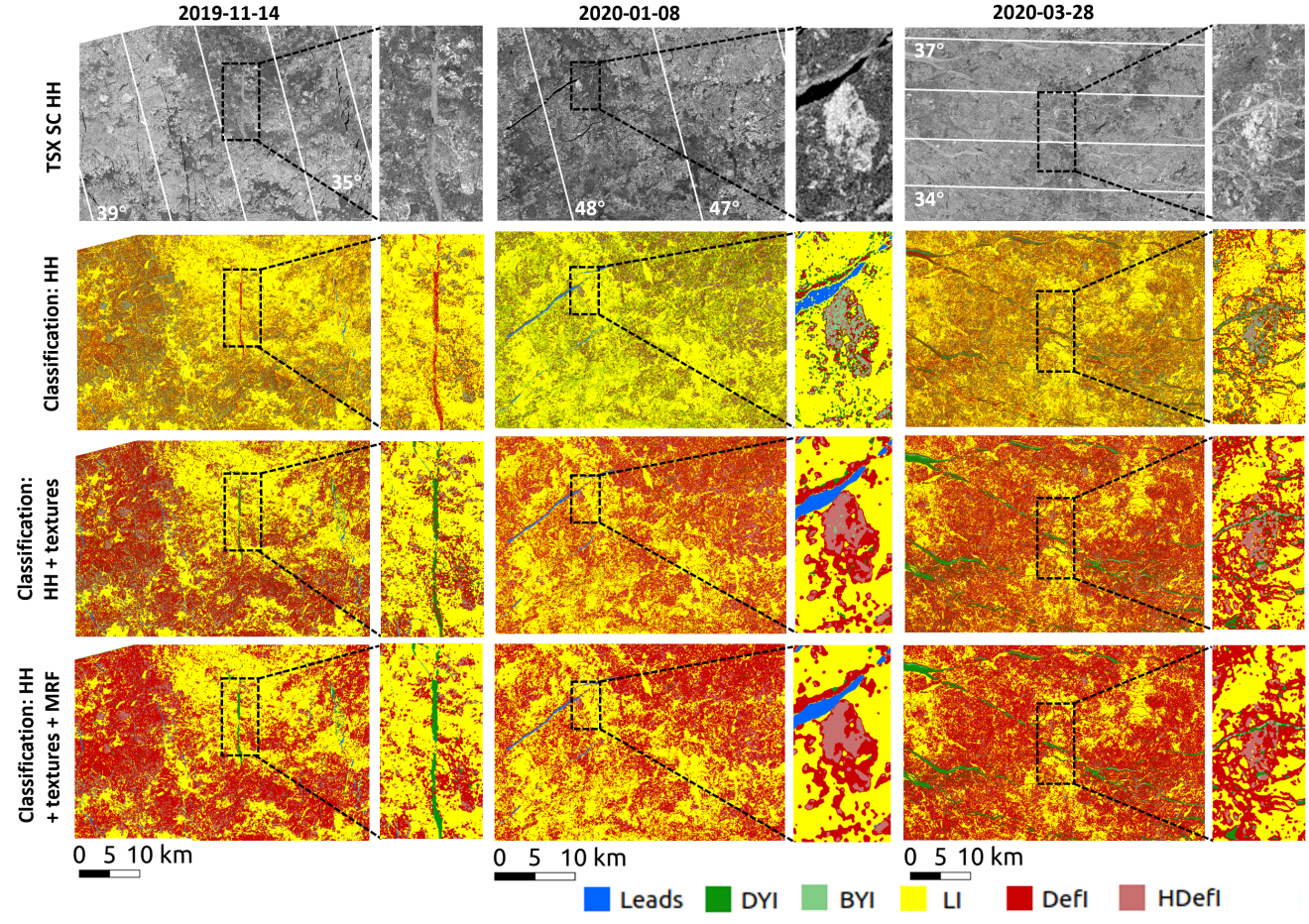

Figure 7. Example TSX SC scenes and classification maps using the GIA classifier trained with HH intensities only, HH intensities and the optimal texture measures, and additionally with MRF contextual smoothing applied, for 3 dates across the time series. All HH subsets are scaled by the same range of intensities, with IAs shown as contours.

these issues. It can be seen that rougher ice (deeper blue) along the transects mostly correctly correspond to areas classified as DefI or HDefI, and smoother ice (lighter blue) to LI (Fig. 10(a)).

Additionally, a classification is conducted on sea ice roughness transects (into LI, DefI and HDefI) for comparison with the SAR-based classification (details of the method shown in Itkin et al. in review), which is shown in Fig. 10(a) on top of HH intensities in the same color scale as the SAR-based classification. In areas of mostly smooth FYI and SYI (outside the Fortress), sea ice roughness is classified with a threshold of 0.2 m into LI (yellow) and DefI (dark red), corresponding well with LI and DefI in the SAR-based classification result. Inside the Fortress, sea ice roughness is classified using the same threshold into DefI (dark red) and heavily HDefI (light red), again showing similar spatial distribution to DefI and HDefI on the SAR-based classification maps.

https://doi.org/10.5194/tc-2022-86
Preprint. Discussion started: 3 May 2022

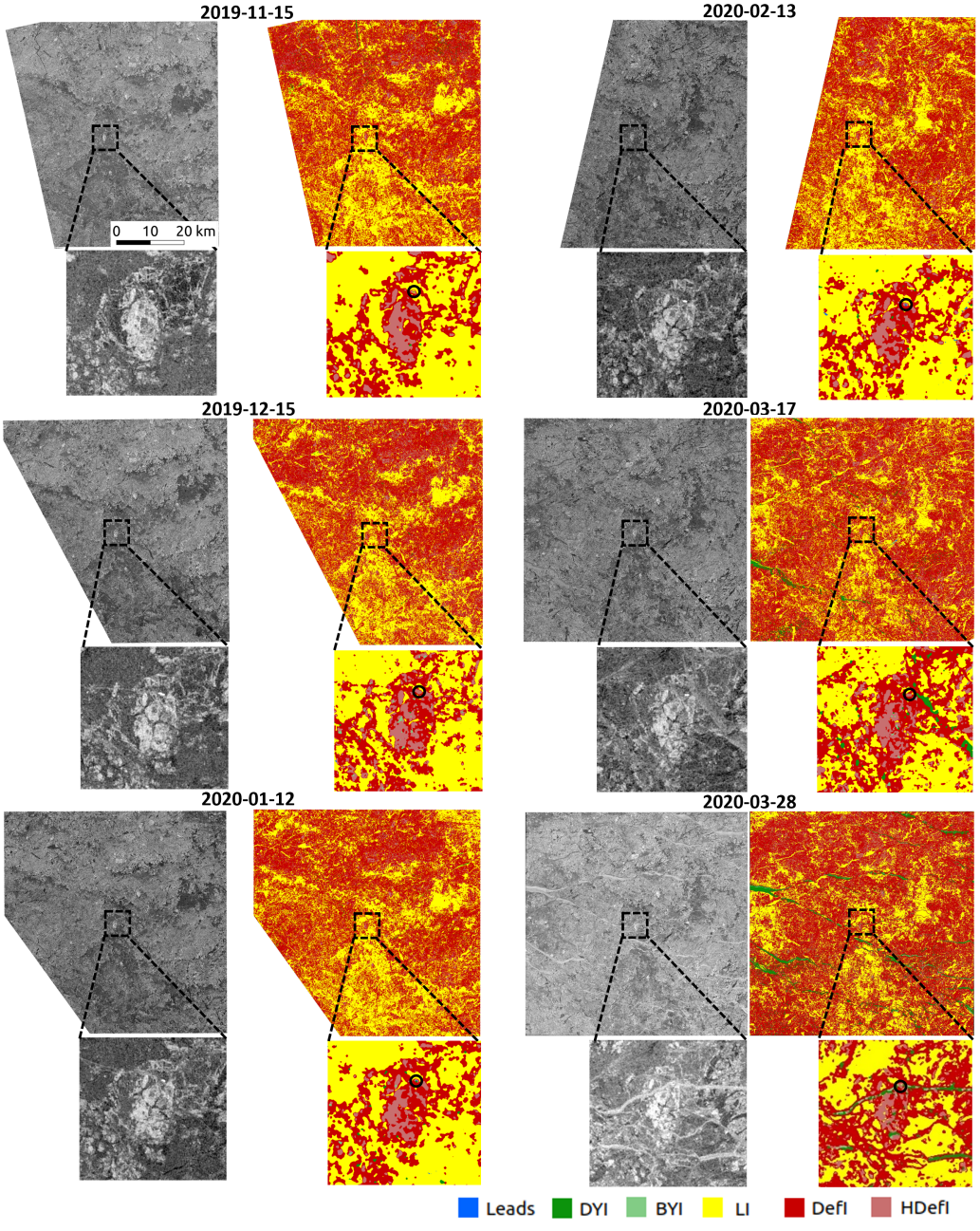

Figure 8. Classification maps of TSX SC scenes near the middle of each month in the time series, and zoomed-in subsets focusing on the MOSAiC ice floe. The last scene in the time series is also shown. On the zoomed-in classification maps, black circles indicate the position of Polarstern. All HH scenes are scaled by the same range of intensities.

https://doi.org/10.5194/tc-2022-86
Preprint. Discussion started: 3 May 2022

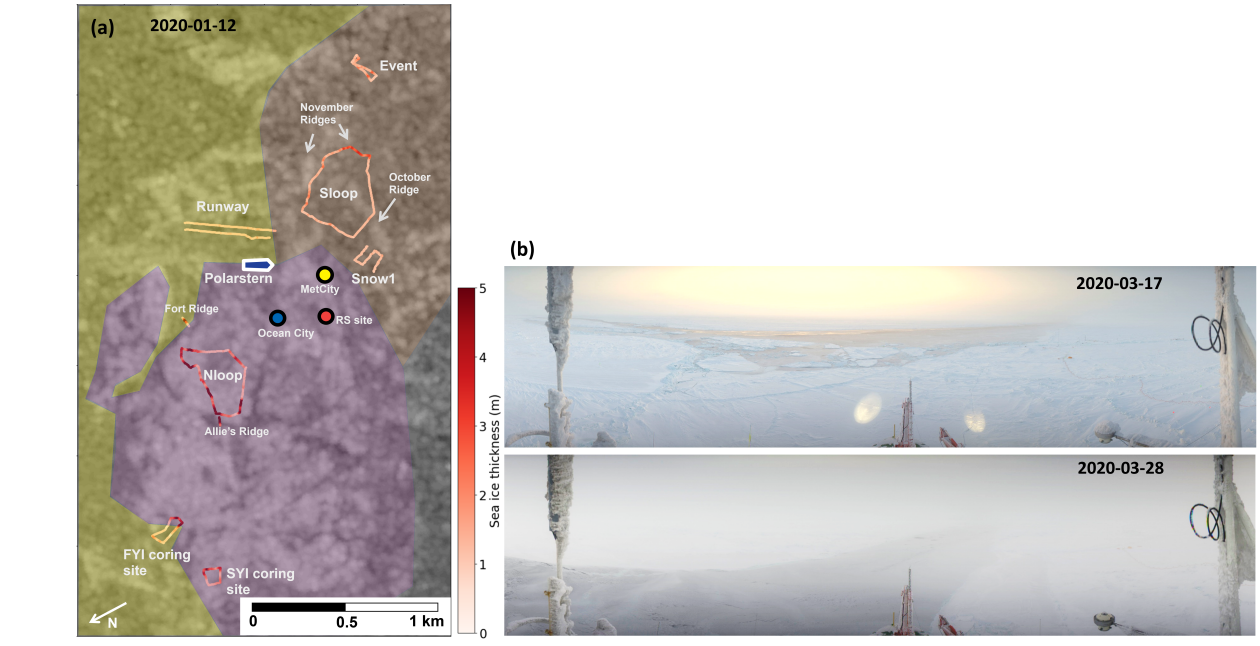

Figure 9. (a) Manual sea ice classification of the CO overlaid on a RS2 SCW scene (HH) on 2020.01.12 - yellow: FYI; purple: rough SYI; red: ponded SYI; Polarstern, weather stations, and transects with sea ice thickness measurements are also shown; (b) Panoramic photos taken from Polarstern on 2020.03.17 and 2020.03.28.

Two repeated transects are available on all dates in Fig. 10(a): the Southern and Northern transect loops, or 'Sloop' and 'Nloop'. Sloop is located in the aforementioned ponded SYI area, and crosses a mixture of rough SYI and smooth refrozen melt pond surface which have similar X-band backscatter to LI, while Nloop is located within the Fortress and thus is a transect of predominantly heavily deformed SYI (Itkin et al., in review). These observations are mostly correctly shown both in our classification map and the classified transects. The transect 'runway', established on a LI surface to supplement FYI sampling in the CO, is also consistently classified as LI in both classifications in Fig. 10(a).

As sea ice roughness calculated from ice thickness represents both surface and bottom roughness, apparent mismatch between the two classifications can be seen in the transect Sloop on the 'November ridges,' most notably on 2020.01.12, as pointed out by arrows in Fig. 10(a). In the southern part of Sloop (arrow to the right) where ice is relatively smooth but thick, high roughness is calculated from the transect (classified as DefI), while TSX SC HH intensities are low (thus classified as LI), presumably due to the dominance of ice-bottom roughness. On the contrary, in the northern part of Sloop (arrow to the left), high HH intensities are observed indicating rough ice surface (classified as DefI), while ice roughness calculated from the transect is low and mostly classified as LI, most likely due to low standard deviations calculated from the relatively thin ice (Fig. 9(a)) in this area.

The percentages of correct correspondence between this *in situ* ice roughness classification and the SAR-based classification for repeated transects through the time series is shown in Fig. 10(b). Corresponding to a specific *in situ* ice roughness classi-

https://doi.org/10.5194/tc-2022-86
Preprint. Discussion started: 3 May 2022

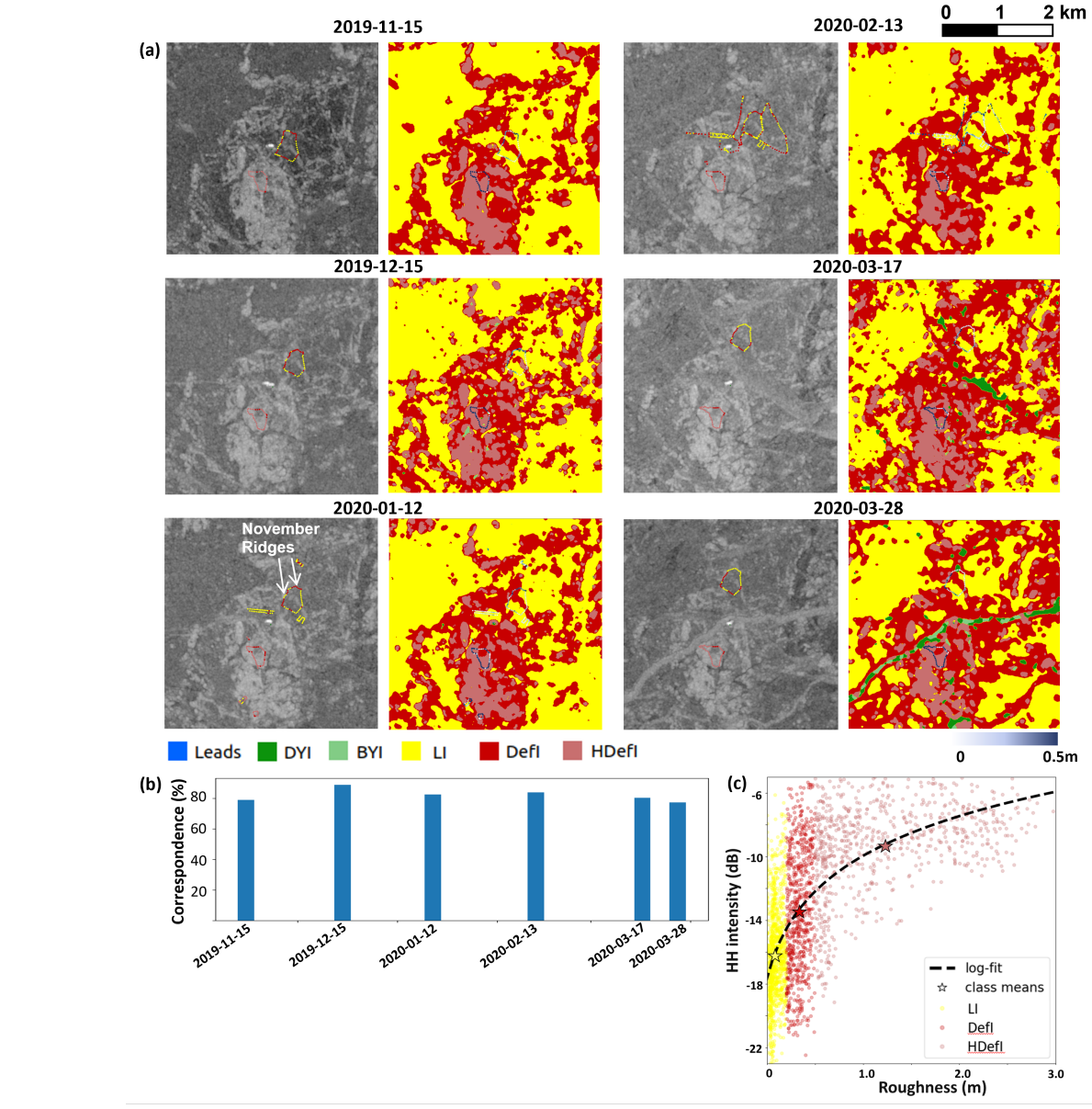

Figure 10. Sea ice roughness in transects (in blue) overlaid on classification maps, and classification of sea ice roughness (in the same color scheme as the SAR-based classification) overlaid on TSX SC HH intensities, in several transects within a 4 km×4 km square around Polarstern for the same dates as Fig. 8; (b) percentage of correspondence between SAR-based and sea ice thickness-based classification of ice roughness in repeated transects in the CO; (c) scatter plot of HH intensities vs. sea ice roughness in repeated transects in the CO, grouped by their corresponding class labels from the SAR-based classification.

https://doi.org/10.5194/tc-2022-86
Preprint. Discussion started: 3 May 2022

fication data point, the SAR-based ice classification is counted as 'correct' if the ice class of at least one TSX SC pixel in its surrounding 4×4 pixel window reports the same class. Good correspondence is found between the two types of classification, with the percentages of 'correctly' classified SAR pixels being consistently near or over 80%.

Finally, we demonstrate the relationship between HH intensities and sea ice roughness for data points in repeated transects in Fig. 10(c), grouped by class labels from the SAR-based classification result. An apparent logarithmic fit can be seen, where the points representing mean roughness and intensities for the 3 thick ice classes (LI, DefI and HDefI, shown in stars) are very close to the fitted curve. This indicates that TSX SC HH intensities are controlled largely by sea ice roughness for the training scenes, which, together with the good correspondence between the SAR-based and *in situ* ice roughness classifications, justifies our chosen classification scheme which separates thick ice into different degrees of deformation. Previous studies have also found winter sea ice roughness to be the dominant factor of C- and L-band SAR intensities for specific channels (e.g., Dierking and Dall 2007; Gegiuc et al. 2018; Cafarella et al. 2019; Segal et al. 2020). As mentioned before, both surface and bottom roughness contribute to the variation in the calculated sea ice roughness, presumably contributing to the relatively wide spread of the scatter plot.

3.3.2 Temporal development of ice class fractions

Areal fractions of different classes in subsets A (solid lines) and B (dashed lines) for all scenes in the time series are shown in Fig. 11(a) and (b). Leads, DYI and BYI are combined into a 'lead ice' category, representing areas of ice opening. The lead ice fraction of a certain scene depends on where the ice openings are within their 'life cycles,' i.e., typically from open water to nilas, young ice with various levels of SAR backscatter intensities, and eventually FYI (in our classification scheme from leads to DYI, BYI, DYI and then LI). For example, a major divergence event occurred from 2020.02.26 to 2020.02.29, resulting in a long ice opening on 2020.02.29 in subset A (not shown) which is not registered in Fig. 11(b) due to its similar intensities and textures to LI.

Relative proportions of LI vs. DefI and HDefI are reasonably consistent through the time series (Fig. 11(a)). Lead ice fractions in subset A are generally higher than subset B, indicating consistently more ice openings captured in subset A, which is considerably larger than subset B (Fig. 11(b)). Several peaks of lead ice fraction are visible through the time series, most notably in mid-late November and mid-December 2019, early January and early and late February 2020. Starting from early March 2020, lead ice fractions remain high throughout the month for both subsets. During this period, ice openings can be consistently visually observed in the scenes. A major ice opening event occurred on 2020.03.28 (Fig. 8), where lead ice fraction reached 4.98% for subset A. This event persisted through early April. A more detailed examination of the ice opening events is conducted by comparing the class fractions to indicators of ice openings from *in situ* data derived in this and other MOSAiC studies:

1. Areal change between buoys (Fig. 11(b), orange): the area between 4 selected buoys (P103, P193, P195 and P204) surrounding the CO (Bliss et al., 2021) are calculated every 3 hours, partially representing events of divergence and convergence. Similar peaks in this areal change can be seen in mid-late November to those of the lead ice fractions (Fig. 11(b)). The area also exhibit frequent changes through March, indicating frequent short-lived ice openings between the buoys. The sharp decrease

https://doi.org/10.5194/tc-2022-86
Preprint. Discussion started: 3 May 2022

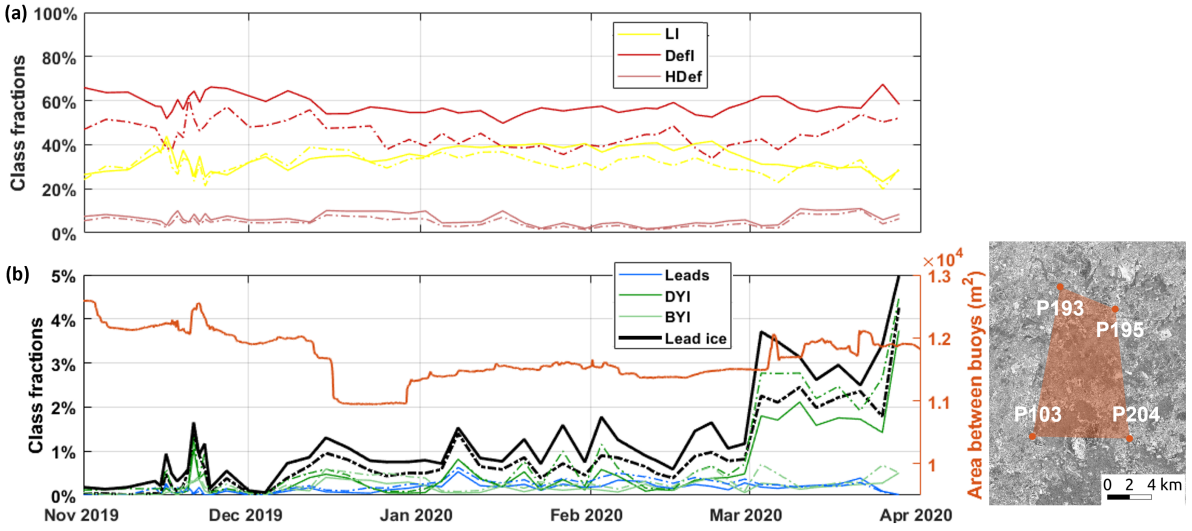

Figure 11. Fractions of (a) FYI and MYI, and (b) lead ice, over the time series. In (a) and (b), solid lines represent class fractions derived from subset A, while dashed lines represent those from subset B. Areas between 4 buoys surrounding the CO (names and positions shown for 2019.11.01) over the time series are also plotted in (b).

in the area starting from 2019.12.15, caused by a large-scale shearing event across the entire extent of subset A lasting through 2019.12.23, leads to mildly increased lead ice fractions in mid-December (Fig. 11(b)). The area between the buoys remain relatively constant in other periods in the time series.

2. Other MOSAiC studies: several peaks of lead ice fractions have good correspondence to lead fractions generated from optical satellite observation (Reiser et al. 2020, reported in Krumpen et al. (2021)). Lead fractions within a 50 km radius from the CO show prominent peaks in early-mid December, early February and early and late March, matching those given in Fig. 11(b). No usable lead fraction is produced for mid-late November and mid-late March, but prominent divergence-convergence events can be seen in mid-late November and late March as obtained from S1 sea ice drift data (Krumpen et al., 2021). In a recent study of sea ice classification on TSX dual-pol StripMap images (SM, 54 km×16 km at 3.5m resolution) using convolutional neural networks and a conditional random field, Kortum et al. (2022) also identifies prominent rise in young ice class fractions in the 3 km×3 km area around Polarstern in late November 2019 and late March 2020. Abrupt and prominent changes in wind speed and direction were recorded from Polarstern in mid-late November 2019 and mid- to late-March 2020 (Itkin et al., in review), which likely contributed to lead opening events shown in Fig. 11(b). These comparisons demonstrate that the classified time series is valuable as an indicator of ice openings, and thus a good reference to studying associated physical processes through the expedition in a larger spatial scale than the previously derived MOSAiC sea ice classification product (Kortum et al., 2022).

https://doi.org/10.5194/tc-2022-86
Preprint. Discussion started: 3 May 2022

3.4 Limitations and future steps

The current classifier has limited capability in detecting linear young ice areas that are narrower than the texture window size used. This is an inevitable outcome of texture-based classification, which contributes to our objective to minimize texture windows. The leads class are mostly fully represented in the classification maps, as it is classified with HH intensities only. The inherent scalloping and inter-scan banding issues for ScanSAR scenes can be seen in the TSX SC scenes, and is more prominently shown in the texture images. These issues are more pronounced in scenes with IAs of higher than 50°, and affects the classification results, most notably leading to mis-classification between the difficult class pairs. In this study, this issue is partially remedied by the MRF contextual smoothing process. If future applications necessitate the usage of TSX SC scenes with obvious sensor artifacts, additional steps should be taken to remedy these issues using procedures proposed by previous studies (e.g., Iqbal et al. 2012; Yang et al. 2020), as used in e.g., Zhang et al. (2019). Also, no continuous *in situ* observation of thin ice is available to provide detailed information on the evolution of these areas through the time series. Sea ice roughness derived from *in situ* sea ice thickness measurements is calculated on a different spatial scale than the classification maps, represents both surface and bottom ice roughness, and suffers from potential co-location errors due to sea ice rotation and deformation. Therefore, the utilization of ice surface roughness data calculated from air-borne and ground-based laser scanners is desirable in future studies as a stronger validation of ice classification.

This study has focused on the freezing season during the MOSAiC expedition. Reasonable classification of April scenes are achievable through individually fitted classifiers with different texture parameters, but a consistent classifier is not available due to the small IA range of April scenes for which separate training is needed in the framework of the proposed workflow. Future steps will extend the study period into the summer season to examine the seasonality of TSX SC textures on sea ice, and its effects on texture-based sea ice classification. This seasonality analysis is valuable in providing a comprehensive perspective of the change in IA dependencies of TSX SC textures from freezing to melting. Further application of the proposed classification workflow can be extended to dual-polarization TSX SC data, utilizing information from the additional VV channel. Similarly, studies of C-band SAR-based sea ice classification have demonstrated that per-class IA correction is still necessary for the HV channel, despite the weaker IA dependencies of its intensities compared to HH due to much more pronounced influence from noise (Aldenhoff et al., 2020; Lohse et al., 2021).

For future studies on texture-based sea ice classification, more detailed quantification of the correspondence between GLCM textures and sea ice surface properties should be conducted, following previous studies (e.g., Baraldi and Parmiggiani 1995; Soh and Tsatsoulis 1999). Also, as mentioned earlier, previous studies of SAR texture-based sea ice classification has achieved sea ice type separation in various physical window sizes. Therefore, further investigation into better including multi-scale textural information (by varying window and displacement step sizes) is desirable, which can potentially capture and utilize both micro- and macro-scale sea ice textures (e.g., Soh and Tsatsoulis 1999; Leigh et al. 2014). Finally, although GLCM textures have been demonstrated to be among the most powerful tools for texture-based classification (Hall-Beyer, 2017; Zakhvatkina et al., 2019), it is still valuable to investigate IA dependencies and utilization of other types of image textures previously used for sea ice classification, e.g., first-order textures, image moments, MRF-based, wavelet transformed-based, variogram-based, and Gray

https://doi.org/10.5194/tc-2022-86
Preprint. Discussion started: 3 May 2022

Level Dependence Matrix (GLDM) based textures, etc. (Conners and Harlow, 1980; Unser, 1995; Clausi, 2001; Clausi and Yu, 2004; Sanden and Hoekman, 2005; Bogdanov et al., 2007; Komarov and Buehner, 2017; Gegiuc et al., 2018; Scharien and Nasonova, 2020).

4 Conclusions

This study demonstrates per-class IA dependencies of HH intensities and GLCM textures calculated from TSX SC data, based on scenes acquired during the winter months of the MOSAiC expedition. Linear IA dependencies of HH intensities in dB are shown to be generally lower than C-band data, but between-class IA slope differences still necessitate per-class correction of the IA effect. In constrained IA ranges, GLCM textures calculated from dB intensities also exhibit linear dependency to IA, and is thus suitable for use by the GIA classifier. The leads class has a relatively wide scatter in HH intensities and textures vs. IAs resulting in weak linear dependency, and is thus retrieved from a separate classification based on HH intensities only. A texture parameter selection process based on statistical separability between class distributions has determined the optimal texture combination to be used is COR, DIS, ENG, ENP, HOM, MAX and SMA (see Table 1 for definitions) at a window size of 9 pixels. With a classification scheme designed for the task of one-band classification, the GIA classifier is trained using HH intensities and textures to account for different IA dependencies of different ice classes, and used to classify the time series. Qualitative (through visual inspection of resulting classification maps) and quantitative (using classification accuracies calculated from validation polygons) assessments show that the inclusion of GLCM textures brings vast improvements in classification performance compared to HH intensity-based classification, and is essential in classifying TSX SC data. The application of MRF contextual smoothing further refines the classification result while preserving maximum spatial details, leading to significantly increased classification accuracies. Good correspondence is found between the classification result and sea ice roughness calculated from *in situ* sea ice thickness measurements. The classified time series show reasonably consistent fractions of LI vs. DefI and HDefI through the time series. Lead ice fractions derived from the classification result correspond well with other indicators of ice openings derived in this and previous studies. This suggests that the classified time series can serve as a reliable reference of the changing sea ice conditions and associated physical processes during the expedition within the spatial scale of TSX SC scenes (approximately 100×150 km). This study provides valuable information on the utilization of per-class IA dependencies of TSX SC intensities and GLCM textures in classifying sea ice, and a classification product of a broad area surrounding the MOSAiC ice camp that can potentially facilitate future MOSAiC sea ice studies and modeling efforts.

Data availability. The classified time series in subset A is available as projected GeoTIFFs (in EPSG:3575) here: https://www.dropbox.com/sh/edx4eq2oux0fqdg/AAB5CXZ8ReTwZNpXe48mpoZYa?dl=0. Correspondence between pixel values and class labels: 3: leads; 5: DYI; 6: BYI; 7: LI; 9: DefI; 10: HDefI.

https://doi.org/10.5194/tc-2022-86
Preprint. Discussion started: 3 May 2022

Author contributions. PI, SSI, APD, MJ, and GS were involved in project administration and supervision. All co-authors were involved in the conceptualization of the study. SSI was responsible for TSX SC data acquisition. WG was responsible for data curation, methodology designing, formal analysis, and result visualization. PI conducted the analysis on sea ice surface roughness using sea ice thickness measurements from MOSAiC, and provided the manual sea ice classification map surrounding the CO and the time series of areal change between the buoys. APD provided his codes and knowledge of MRF contextual smoothing. WG prepared the manuscript, with contributions from all co-authors in reviewing and editing.

Competing interests. No competing interests are present.

Acknowledgements. The authors would like to thank all persons involved in the expedition of the Research Vessel Polarstern during Multidisciplinary Drifting Observatory for the Study of the Arctic Climate (MOSAiC) in 2019–2020 as listed in Nixdorf et al. (2021). This work was supported by the Research Council of Norway (RCN) projects: Sea Ice Deformation and Snow for an Arctic in Transition (SIDRiFT) (287871), Center for Integrated Remote Sensing and Forecasting for Arctic Operations (CIRFA) (237906), and Project Oil spill and newly formed sea ice detection, characterization, and mapping in the Barents Sea using remote sensing by SAR (OIBSAR) (280616). SSI and GS are supported by the Deutsche Forschungsgemeinschaft (DFG) through the Project "MOSAiCmicrowaveRS" (Grant 420499875).

Data used in this article were produced as part of the International Multidisciplinary Drifting Observatory for the Study of the Arctic Climate (MOSAiC) with the tag MOSAiC20192020 and Project_ID: AWI_PS122_00. TerraSAR-X images used in this study were acquired using the TerraSAR-X AO OCE3562_4 (PI: SS). RADARSAT-2 data was provided by NSC/KSAT under the Norwegian-Canadian Radarsat agreement 2019 and 2020. Sentinel-1 data is publicly available from the Copernicus Open Access Hub (https://scihub.copernicus.eu/, last access: Oct 2021; European Space Agency 2021). The OSI SAF global sea ice type product (OSI-403-d) is publicly available from https://osi-saf.eumetsat.int/products/osi-403-d (last access: Oct 2021; OSI SAF 2019). The NSIDC IST dataset (MOD29/MYD29) is publicly available from https://nsidc.org/data/MOD29 (last access: Oct 2021; Hall and Riggs. 2021).

https://doi.org/10.5194/tc-2022-86
Preprint. Discussion started: 3 May 2022

References

Aldenhoff, W., Eriksson, L. E., Ye, Y., and Heuze, C.: First-Year and Multiyear Sea Ice Incidence Angle Normalization of Dual-Polarized Sentinel-1 SAR Images in the Beaufort Sea, IEEE Journal of Selected Topics in Applied Earth Observations and Remote Sensing, 13, 1540–1550, https://doi.org/10.1109/JSTARS.2020.2977506, 2020.

Alonso, M. C., Malpica, J. A., and de Agirre, A. M.: Consequences of the Hughes phenomenon on some classification techniques, in: Proceedings of the ASPRS 2001 annual conference, pp. 1–5, 2011.

Baraldi, A. and Parmiggiani, F.: Investigation of the textural characteristics associated with gray level cooccurrence matrix statistical parameters, IEEE Transactions on Geoscience and Remote Sensing, 33, 293–304, https://doi.org/10.1109/36.377929, 1995.

Barber, D. G. and LeDrew, E. F.: SAR Sea Ice Discrimination Using Texture Statistics: A Multivariate Approach Photogrammetric Engineering and Remote Sensing, Photogrammetric Engineering and Remote Sensing, 57 (4), 385–395, 1991.

Barber, D. G., Ehn, J. K., Pućko, M., Rysgaard, S., Deming, J. W., Bowman, J. S., Papakyriakou, T., Galley, R. J., and Søgaard, D. H.: Frost flowers on young Arctic sea ice: The climatic, chemical, and microbial significance of an emerging ice type, Journal of Geophysical Research: Atmospheres, 119, 11,511–593,612, https://doi.org/https://doi.org/10.1002/2014JD021736, 2014.

Bliss, A., Hutchings, J., Anderson, P., Anhaus, P., and Jakob Belter, H.: Sea ice drift tracks from the Distributed Network of autonomous buoys deployed during the Multidisciplinary drifting Observatory for the Study of Arctic Climate (MOSAiC) expedition 2019 - 2021, https://doi.org/10.18739/A2Q52FD8S, 2021.

Bogdanov, A. V., Sandven, S., Johannessen, O. M., Alexandrov, V. Y., and Bobylev, L. P.: Multi-sensor approach to automated classification of sea ice image data, Image Processing for Remote Sensing, 43, 293–324, https://doi.org/10.1201/9781420066654.ch13, 2007.

Cafarella, S. M., Scharien, R., Geldsetzer, T., Howell, S., Haas, C., Segal, R., and Nasonova, S.: Estimation of Level and Deformed First-Year Sea Ice Surface Roughness in the Canadian Arctic Archipelago from C- and L-Band Synthetic Aperture Radar, Canadian Journal of Remote Sensing, 45, 457–475, https://doi.org/10.1080/07038992.2019.1647102, 2019.

Clausi, D. A.: Comparison and fusion of co-occurrence, Gabor and MRF texture features for classification of SAR sea-ice imagery, Atmosphere - Ocean, 39, 183–194, https://doi.org/10.1080/07055900.2001.9649675, 2001.

Clausi, D. A. and Yu, B.: Comparing cooccurrence probabilities and Markov random fields for texture analysis of SAR sea ice imagery, IEEE Transactions on Geoscience and Remote Sensing, 42, 215–228, https://doi.org/10.1109/TGRS.2003.817218, 2004.

Conners, R. W. and Harlow, C. A.: A theoretical comparison of texture algorithms, IEEE Transactions on Pattern Analysis and Machine Intelligence, PAMI-2, 204–222, https://doi.org/10.1109/TPAMI.1980.4767008, 1980.

Daniel, W. W.: Applied nonparametric statistics, Boston (Mass.) : PWS-KENT, 2nd ed. edn., http://lib.ugent.be/catalog/rug01:000283035, 1990.

Dierking, W.: Mapping of Different Sea Ice Regimes Using Images From Sentinel-1 and ALOS Synthetic Aperture Radar, IEEE Transactions on Geoscience and Remote Sensing, 48, 1045–1058, https://doi.org/10.1109/TGRS.2009.2031806, 2010.

Dierking, W. and Dall, J.: Sea-ice deformation state from synthetic aperture radar imagery - Part I: Comparison of C- and L-B and and different polarization, IEEE Transactions on Geoscience and Remote Sensing, 45, 3610–3621, https://doi.org/10.1109/TGRS.2007.903711, 2007.

Doulgeris, A. P.: An automatic U-distribution and markov random field segmentation algorithm for PolSAR images, IEEE Transactions on Geoscience and Remote Sensing, 53, 1819–1827, https://doi.org/10.1109/TGRS.2014.2349575, 2015.

European Space Agency: SNAP - ESA Sentinel Application Platform v7.0.4, http://step.esa.int, 2020.

European Space Agency: Copernicus Sentinel data, https://scihub.copernicus.eu/TS2, 2021.

Ferro, C. J. S. and Warner, T. A.: Scale and texture in digital image classification, Photogrammetric Engineering Remote Sensing, 68, 51–63, 2002.

Fritz, T., Eineder, M., Brautigam, B., Schattler, B., Balzer, W., Buckreuss, S., and Werninghaus, B.: TerraSAR-X ground segment, basic product specification document, Tech. rep., DLR, 2013.

Gegiuc, A., Similä, M., Karvonen, J., Lensu, M., Mäkynen, M., and Vainio, J.: Estimation of degree of sea ice ridging based on dual-polarized C-band SAR data, The Cryosphere, 12, 343–364, https://doi.org/10.5194/tc-12-343-2018, 2018.

Gorelick, N., Hancher, M., Dixon, M., Ilyushchenko, S., Thau, D., and Moore, R.: Google Earth Engine: Planetary-scale geospatial analysis for everyone, Remote Sensing of Environment, 202, 18–27, https://doi.org/10.1016/j.rse.2017.06.031, 2017.

Guo, W., Itkin, P., Lohse, J., Johansson, M., and Doulgeris, A. P.: Cross-platform classification of level and deformed sea ice considering per-class incident angle dependency of backscatter intensity, The Cryosphere, 16, 237–257, https://doi.org/10.5194/tc-16-237-2022, 2022.

Hall, D. K. and Riggs., G. A.: MODIS/Terra Sea Ice Extent 5-Min L2 Swath 1km, Version 61, https://doi.org/https://doi.org/10.5067/MODIS/MOD29.061, 2021.

Hall-Beyer, M.: GLCM texture tutorial, http://www.fp.ucalgary.ca/mhallbey/, 2008.

Hall-Beyer, M.: Practical guidelines for choosing GLCM textures to use in landscape classification tasks over a range of moderate spatial scales, International Journal of Remote Sensing, 38, 1312–1338, https://doi.org/10.1080/01431161.2016.1278314, 2017.

Haralick, R., Shanmugan, K., and Dinstein, I.: Textural features for image classification, https://doi.org/10.1109/TSMC.1973.4309314, 1973.

Hendricks, S., Itkin, P., Ricker, R., Webster, M., von Albedyll, L., Rohde, J., Raphael, I., Jaggi, M., and Arndt, S.: GEM-2 quicklook total thickness measurements from the 2019-2020 MOSAiC expedition, https://doi.org/PDI-31126, 2022.

Holmes, Q. A., Nuesch, D. R., and Shuchman, R. A.: Textural Analysis and Real-Time Classification of Sea-Ice Types Using Digital SAR Data, IEEE Transactions on Geoscience and Remote Sensing, GE-22, 113–120, https://doi.org/10.1109/TGRS.1984.350602, 1984.

Hughes, G.: On the mean accuracy of statistical pattern recognizers, IEEE transactions on information theory, 14, 55–63, https://doi.org/10.1109/TIT.1968.1054102, 1968.

Iqbal, M., Chen, J., Yang, W., Wang, P., and Sun, B.: Kalman filter for removal of scalloping and inter-scan banding in scansar images, Progress in Electromagnetics Research, 132, 443–461, https://doi.org/10.2528/PIER12082107, 2012.

Isleifson, D., Hwang, B., Barber, D. G., Scharien, R. K., and Shafai, L.: C-band polarimetric backscattering signatures of newly formed sea ice during fall freeze-up, IEEE Transactions on Geoscience and Remote Sensing, 48, 3256–3267, https://doi.org/10.1109/TGRS.2010.2043954, 2010.

Isleifson, D., Galley, R. J., Firoozy, N., Landy, J. C., and Barber, D. G.: Investigations into frost flower physical characteristics and the C-band scattering response, Remote Sensing, 10, 1–16, https://doi.org/10.3390/rs10070991, 2018.

https://doi.org/10.5194/tc-2022-86
Preprint. Discussion started: 3 May 2022

Itkin, P., Hendricks, S., Webster, M., Albedyll, L. V., Arndt, S., Divine, D., Jaggi, M., Oggier, M., Raphael, I., Ricker, R., Rohde, J., Schneebeli, M., and Liston, G.: Sea ice and snow mass balance from transects in the MOSAiC Central Observatory, Elementa: Science of the Anthropocene, in review.

Johansson, A. M., Brekke, C., Spreen, G., and King, J. A.: X-, C-, and L-band SAR signatures of newly formed sea ice in Arctic leads during winter and spring, Remote Sensing of Environment, 204, 162–180, https://doi.org/10.1016/j.rse.2017.10.032, 2018.

Komarov, A. S. and Buehner, M.: Automated Detection of Ice and Open Water from Dual-Polarization RADARSAT-2 Images for Data Assimilation, IEEE Transactions on Geoscience and Remote Sensing, 55, 5755–5769, https://doi.org/10.1109/TGRS.2017.2713987, 2017.

Kortum, K., Singha, S., and Spreen, G.: Robust Multiseasonal Ice Classification From High-Resolution X-Band SAR, IEEE Transactions on Geoscience and Remote Sensing, 60, 1–12, https://doi.org/10.1109/TGRS.2022.3144731, 2022.

Krumpen, T. and Sokolov, V.: The Expedition AF122/1: Setting up the MOSAiC Distributed Network in October 2019 with Research Vessel AKADEMIK FEDOROV, Berichte zur Polar-und Meeresforschung= Reports on polar and marine research, 744, 2020.

Krumpen, T., Birrien, F., Kauker, F., Rackow, T., Von Albedyll, L., Angelopoulos, M., Jakob Belter, H., Bessonov, V., Damm, E., Dethloff, K., Haapala, J., Haas, C., Harris, C., Hendricks, S., Hoelemann, J., Hoppmann, M., Kaleschke, L., Karcher, M., Kolabutin, N., Lei, R., Lenz, J., Morgenstern, A., Nicolaus, M., Nixdorf, U., Petrovsky, T., Rabe, B., Rabenstein, L., Rex, M., Ricker, R., Rohde, J., Shimanchuk, E., Singha, S., Smolyanitsky, V., Sokolov, V., Stanton, T., Timofeeva, A., Tsamados, M., and Watkins, D.: The MOSAiC ice floe: Sediment-laden survivor from the Siberian shelf, The Cryosphere, 14, 2173–2187, https://doi.org/10.5194/tc-14-2173-2020, 2020.

Krumpen, T., Albedyll, L. V., Goessling, H. F., Hendricks, S., Juhls, B., Katlein, C., Tian-kunze, X., Ricker, R., Rostosky, P., Rückert, J., and Singha, S.: MOSAiC drift expedition from October 2019 to July 2020 : sea ice conditions from space and comparison with previous years, The Cryosphere, pp. 3897–3920, 2021.

Leigh, S., Wang, Z., and Clausi, D. A.: Automated ice-water classification using dual polarization SAR satellite imagery, IEEE Transactions on Geoscience and Remote Sensing, 52, 5529–5539, https://doi.org/10.1109/TGRS.2013.2290231, 2014.

Liu, H., Li, X. M., and Guo, H.: The Dynamic Processes of Sea Ice on the East Coast of Antarctica-A Case Study Based on Spaceborne Synthetic Aperture Radar Data from TerraSAR-X, IEEE Journal of Selected Topics in Applied Earth Observations and Remote Sensing, 9, 1187–1198, https://doi.org/10.1109/JSTARS.2015.2497355, 2016.

Liu, H., Guo, H., and Liu, G.: A Two-Scale Method of Sea Ice Classification Using TerraSAR-X ScanSAR Data During Early Freeze-Up, IEEE Journal of Selected Topics in Applied Earth Observations and Remote Sensing, 14, 10 919–10 928, https://doi.org/10.1109/JSTARS.2021.3122546, 2021.

Lohse, J., Doulgeris, A. P., and Dierking, W.: Mapping sea-ice types from Sentinel-1 considering the surface-type dependent effect of incidence angle, Annals of Glaciology, pp. 1–11, https://doi.org/10.1017/aog.2020.45, 2020.

Lohse, J., Doulgeris, A. P., and Dierking, W.: Incident Angle Dependence of Sentinel-1 Texture Features for Sea Ice Classification (in review), Remote Sensing, 13, https://www.mdpi.com/2072-4292/13/4/552, 2021.

Mahmud, M. S., Geldsetzer, T., Howell, S. E., Yackel, J. J., Nandan, V., and Scharien, R. K.: Incidence angle dependence of HH-polarized C- A nd L-band wintertime backscatter over arctic sea ice, IEEE Transactions on Geoscience and Remote Sensing, 56, 6686–6698, https://doi.org/10.1109/TGRS.2018.2841343, 2018.

Mäkynen, M. and Hallikainen, M.: Investigation of C- and X-band backscattering signatures of Baltic Sea ice, International Journal of Remote Sensing, 25, 2061–2086, https://doi.org/10.1080/01431160310001647697, 2004.

Mäkynen, M. and Juha, K.: Incidence Angle Dependence of First-Year Sea Ice Backscattering Coefficient in Sentinel-1 SAR Imagery over the Kara Sea, IEEE Transactions on Geoscience and Remote Sensing, 55, 6170–6181, https://doi.org/10.1109/TGRS.2017.2721981, 2017.

Mäkynen, M. P., Manninen, A. T., Similä, M. H., Karvonen, J. A., and Hallikainen, M. T.: Incidence angle dependence of the statistical properties of C-band HH-polarization backscattering signatures of the Baltic Sea ice, IEEE Transactions on Geoscience and Remote Sensing, 40, 2593–2605, https://doi.org/10.1109/TGRS.2002.806991, 2002.

Marceau, D. J., Howarth, P. J., Dubois, J. M. M., and Gratton, D. J.: Evaluation of the Grey-Level Co-Occurrence Matrix Method for Land-Cover Classification Using SPOT Imagery, IEEE Transactions on Geoscience and Remote Sensing, 28, 513–519, https://doi.org/10.1109/TGRS.1990.572937, 1990.

Marcel, W., Clauss, K., Valgur, M., and Sølvsteen, J.: Sentinelsat Python API, GNU General Public License v3.0+, https://github.com/sentinelsat/sentinelsat/tree/a551d071f9c5faae09603ec4a3ef9dc3dd3ef833, 2021.

Martin, S., Drucker, R. M., and Fort, M.: A laboratory study of frost flower growth on the surface of young sea ice, Journal of Geophysical Research, 100, 7027–7036, 1995.

Massey Jr, F. J.: The Kolmogorov-Smirnov test for goodness of fit, Journal of the American statistical Association, 46, 68–78, 1951.

Murashkin, D., Spreen, G., Huntemann, M., and Dierking, W.: Method for detection of leads from Sentinel-1 SAR images, Annals of Glaciology, 59, 124–136, https://doi.org/10.1017/aog.2018.6, 2018.

Nicolaus, M., Arndt, S., Birnbaum, G., and Katlein, C.: Visual panoramic photographs of the surface conditions during the MOSAiC campaign 2019/20, https://doi.org/10.1594/PANGAEA.938534, 2021.

Nixdorf, U., Dethloff, K., Rex, M., Shupe, M., Sommerfeld, A., Perovich, D. K., Nicolaus, M., Heuzé, C., Rabe, B., Loose, B., Damm, E., Gradinger, R., Fong, A., Maslowski, W., Rinke, A., Kwok, R., Spreen, G., Wendisch, M., Herber, A., Hirsekorn, M., Mohaupt, V., Frickenhaus, S., Immerz, A., Weiss-Tuider, K., König, B., Mengedoht, D., Regnery, J., Gerchow, P., Ransby, D., Krumpen, T., Morgenstern, A., Haas, C., Kanzow, T., Rack, F. R., Saitzev, V., Sokolov, V., Makarov, A., Schwarze, S., Wunderlich, T., Wurr, K., and Boetius, A.: MOSAiC Extended Acknowledgement, https://doi.org/10.5281/zenodo.5541624, 2021.

OSI SAF: The Sea ice type product of the EUMETSAT Ocean and Sea Ice Satellite Application Facility (OSI SAF), https://osi-saf.eumetsat.int/products/osi-403-d, 2019.

Park, J. W., Korosov, A. A., Babiker, M., Won, J. S., Hansen, M. W., and Kim, H. C.: Classification of sea ice types in Sentinel-1 synthetic aperture radar images, The Cryosphere, 14, 2629–2645, https://doi.org/10.5194/tc-14-2629-2020, 2020.

Reiser, F., Willmes, S., and Heinemann, G.: A New Algorithm for Daily Sea Ice Lead Identification in the Arctic and Antarctic Winter from Thermal-Infrared Satellite Imagery, https://doi.org/10.3390/rs12121957, 2020.

Ressel, R., Frost, A., and Lehner, S.: A Neural Network-Based Classification for Sea Ice Types on X-Band SAR Images, IEEE Journal of Selected Topics in Applied Earth Observations and Remote Sensing, 8, 3672–3680, https://doi.org/10.1109/JSTARS.2015.2436993, 2015.

Sanden, J. J. D. and Hoekman, D. H.: Review of relationships between grey-tone co-occurrence, semivariance, and autocorrelation based image texture analysis approaches, Canadian Journal of Remote Sensing, 31, 207–213, https://doi.org/10.5589/m05-008, 2005.

https://doi.org/10.5194/tc-2022-86
Preprint. Discussion started: 3 May 2022

Scharien, R. K. and Nasonova, S.: Incidence Angle Dependence of Texture Statistics From Sentinel-1 HH-Polarization Images of Winter Arctic Sea Ice, IEEE Geoscience and Remote Sensing Letters, pp. 1–5, https://doi.org/10.1109/LGRS.2020.3039739, 2020.

Segal, R. A., Scharien, R. K., Cafarella, S., and Tedstone, A.: Characterizing winter landfast sea-ice surface roughness in the Canadian Arctic Archipelago using Sentinel-1 synthetic aperture radar and the Multi-angle Imaging SpectroRadiometer, Annals of Glaciology, 61, 284–298, https://doi.org/10.1017/aog.2020.48, 2020.

Shokr, M. E.: Evaluation of second-order texture parameters for sea ice classification from radar images, Journal of Geophysical Research: Oceans, 96, 10 625–10 640, https://doi.org/https://doi.org/10.1029/91JC00693, 1991.

Shupe, M. D., Rex, M., Blomquist, B., Persson, P. O. G., Schmale, J., Uttal, T., Althausen, D., Angot, H., Archer, S., Bariteau, L., Beck, I., Bilberry, J., Bucci, S., Buck, C., Boyer, M., Brasseur, Z., Brooks, I. M., Calmer, R., Cassano, J., Castro, V., Chu, D., Costa, D., Cox, C. J., Creamean, J., Crewell, S., Dahlke, S., Damm, E., de Boer, G., Deckelmann, H., Dethloff, K., Dütsch, M., Ebell, K., Ehrlich, A., Ellis, J., Engelmann, R., Fong, A. A., Frey, M. M., Gallagher, M. R., Ganzeveld, L., Gradinger, R., Graeser, J., Greenamyer, V., Griesche, H., Griffiths, S., Hamilton, J., Heinemann, G., Helmig, D., Herber, A., Heuzé, C., Hofer, J., Houchens, T., Howard, D., Inoue, J., Jacobi, H.-W., Jaiser, R., Jokinen, T., Jourdan, O., Jozef, G., King, W., Kirchgaessner, A., Klingebiel, M., Krassovski, M., Krumpen, T., Lampert, A., Landing, W., Laurila, T., Lawrence, D., Lonardi, M., Loose, B., Lüpkes, C., Maahn, M., Macke, A., Maslowski, W., Marsay, C., Maturilli, M., Mech, M., Morris, S., Moser, M., Nicolaus, M., Ortega, P., Osborn, J., Pätzold, F., Perovich, D. K., Petäjä, T., Pilz, C., Pirazzini, R., Posman, K., Powers, H., Pratt, K. A., Preußer, A., Quéléver, L., Radenz, M., Rabe, B., Rinke, A., Sachs, T., Schulz, A., Siebert, H., Silva, T., Solomon, A., Sommerfeld, A., Spreen, G., Stephens, M., Stohl, A., Svensson, G., Uin, J., Viegas, J., Voigt, C., von der Gathen, P., Wehner, B., Welker, J. M., Wendisch, M., Werner, M., Xie, Z., and Yue, F.: Overview of the MOSAiC expedition: Atmosphere, Elementa: Science of the Anthropocene, 10, 60, https://doi.org/10.1525/elementa.2021.00060, 2022.

Soh, L. K. and Tsatsoulis, C.: Texture analysis of sar sea ice imagery using gray level co-occurrence matrices, IEEE Transactions on Geoscience and Remote Sensing, 37, 780–795, https://doi.org/10.1109/36.752194, 1999.

The Mathworks Inc.: MATLAB R2021b, http://www.mathworks.com/, 2021.

Unser, M.: Texture classification and segmentation using wavelet frames, IEEE Transactions on image processing, 4, 1549–1560, 1995.

WMO: Sea Ice Nomenclature, WMO/OMM/BMO - No. 259, Terminology, Volume I, 1970-2017 edn., 2018.

Yang, W., Li, Y., Liu, W., Chen, J., Li, C., and Men, Z.: Scalloping Suppression for ScanSAR Images Based on Modified Kalman Filter With Preprocessing, IEEE Transactions on Geoscience and Remote Sensing, 59, 7535–7546, https://doi.org/10.1109/tgrs.2020.3034098, 2020.

Zakhvatkina, N., Korosov, A., Muckenhuber, S., Sandven, S., and Babiker, M.: Operational algorithm for ice-water classification on dual-polarized RADARSAT-2 images, The Cryosphere, 11, 33–46, https://doi.org/10.5194/tc-11-33-2017, 2017.

Zakhvatkina, N., Smirnov, V., and Bychkova, I.: Satellite SAR Data-based Sea Ice Classification: An Overview, Geosciences, 9, 152, 2019.

Zakhvatkina, N. Y., Alexandrov, V. Y., Johannessen, O. M., Sandven, S., and Frolov, I. Y.: Classification of sea ice types in ENVISAT synthetic aperture radar images, IEEE Transactions on Geoscience and Remote Sensing, 51, 2587–2600, https://doi.org/10.1109/TGRS.2012.2212445, 2013.

Zhang, L., Liu, H., Gu, X., Guo, H., Chen, J., and Liu, G.: Sea Ice Classification Using TerraSAR-X ScanSAR Data With Removal of Scalloping and Interscan Banding, IEEE Journal of Selected Topics in Applied Earth Observations and Remote Sensing, 12, 589–598, https://doi.org/10.1109/JSTARS.2018.2889798, 2019.